RaFSIP: Parameterizing ice multiplication in models using a machine learning approach

Paraskevi Georgakaki[1] and Athanasios Nenes[2]

[1]École Polytechnique Fédérale de Lausanne
[2]Ecole Polytechnique Fédérale de Lausanne

December 27, 2023

Abstract

Representing single or multi-layered mixed-phase clouds (MPCs) accurately in global climate models (GCMs) is critical for capturing climate sensitivity and Arctic amplification. Ice multiplication, or secondary ice production (SIP), can increase the ice crystal number concentration (ICNC) in MPCs by several orders of magnitude, affecting cloud properties and processes. Here, we propose a machine-learning approach, called Random Forest SIP (RaFSIP), to parameterize the effect of SIP on stratiform MPCs. The RaFSIP scheme uses few input variables available in models and considers rime splintering, ice-ice collisional break-up, and droplet-shattering, operating at temperatures between 0 and -25 @C. The training dataset for RaFSIP was derived from two-year pan-Arctic simulations with the Weather Research and Forecasting (WRF) model with explicit representations of SIP processes. The RaFSIP scheme was evaluated offline against WRF simulation outputs, then integrated within WRF. The parameterization exhibits stable performance over a simulation year, and reproduced predictions of ICNC with explicit microphysics to within a factor of 3. The coupled WRF-RaFSIP scheme can replicate regions of enhanced SIP and accurately map ICNCs and liquid water content, particularly at temperatures above -10 @C. Uncertainties related to the RaFSIP representation of MPCs marginally affected surface cloud radiative forcing in the Arctic, with radiative biases of lower than 3 Wm-2 compared to simulations with explicit SIP microphysics. Training from a few high-resolution model grid points did not limit the predictive skill of RaFSIP, with the approach opening up new avenues for model simplification and process description in GCMs by physics-guided machine learning algorithms.

Hosted file

968242_0_supp_11167696_rxg0xn.docx available at https://authorea.com/users/542999/articles/655698-rafsip-parameterizing-ice-multiplication-in-models-using-a-machine-learning-approach

RaFSIP: Parameterizing ice multiplication in models using a machine learning approach

Paraskevi Georgakaki[1] and Athanasios Nenes[1,2*]

[1]Laboratory of Atmospheric Processes and their Impacts (LAPI), School of Architecture, Civil & Environmental Engineering, Ecole Polytechnique Fédérale de Lausanne, Lausanne, Switzerland.

[2]Center for Studies of Air Quality and Climate Change, Institute of Chemical Engineering Sciences, Foundation for Research and Technology Hellas, Patras, Greece.

[*]Corresponding author: Athanasios Nenes (athanasios.nenes@epfl.ch)

Key Points:

- A random-forest parameterization for secondary ice production is developed using outputs from a high-resolution regional climate simulation.
- The scheme produces tendencies of ice multiplication comparable to the high resolution model with explicit microphysics.
- The scheme can be adjusted to coarse resolutions typical of climate models without loss of computational efficiency and numerical stability.

Abstract

Representing single or multi-layered mixed-phase clouds (MPCs) accurately in global climate models (GCMs) is critical for capturing climate sensitivity and Arctic amplification. Ice multiplication, or secondary ice production (SIP), can increase the ice crystal number concentration (ICNC) in MPCs by several orders of magnitude, affecting cloud properties and processes. Here, we propose a machine-learning approach, called Random Forest SIP (RaFSIP), to parameterize the effect of SIP on stratiform MPCs. The RaFSIP scheme uses few input variables available in models and considers rime splintering, ice-ice collisional break-up, and droplet-shattering, operating at temperatures between 0 and -25 ˚C. The training dataset for RaFSIP was derived from two-year pan-Arctic simulations with the Weather Research and Forecasting (WRF) model with explicit representations of SIP processes. The RaFSIP scheme was evaluated offline against WRF simulation outputs, then integrated within WRF. The parameterization exhibits stable performance over a simulation year, and reproduced predictions of ICNC with explicit microphysics to within a factor of 3. The coupled WRF-RaFSIP scheme can replicate regions of enhanced SIP and accurately map ICNCs and liquid water content, particularly at temperatures above -10 ˚C. Uncertainties related to the RaFSIP representation of MPCs marginally affected surface cloud radiative forcing in the Arctic, with radiative biases of lower than 3 Wm^{-2} compared to simulations with explicit SIP microphysics. Training from a few high-resolution model grid points did not limit the predictive skill of RaFSIP, with the approach opening up new avenues for model simplification and process description in GCMs by physics-guided machine learning algorithms.

Plain Language Summary

Being able to correctly simulate the amount of ice and liquid in clouds is essential for accurate predictions of the cloud radiative forcing in the climatologically-sensitive polar regions. A number of collisional processes between ice and liquid particles in clouds, known as secondary ice production, can significantly enhance the ice crystal number concentrations contained in them. This enhancement is often accompanied by a decrease in the number and mass of liquid cloud droplets, resulting in less opaque clouds to incoming solar radiation, which, in turn, can cause a cloud-induced warming at the surface. Currently most global climate models are missing the description of the most important secondary ice production processes, which can lead to a biased radiative impact of clouds at the surface. To address this, we propose using a machine learning algorithm trained on high-resolution model outputs to include the effect of ice multiplication in large-scale climate models. The machine learning framework effectively captures the physical processes underlying secondary ice production in stratiform clouds using only a few inputs readily available in model frameworks. This approach has the potential to improve model outputs and bring them closer to the observed cloud phase partitioning.

1 Introduction

In the big data and machine learning era, general circulation models (GCMs) remain an indispensable tool for predicting how the Earth system will respond to rising greenhouse gas concentrations (Balaji et al., 2022; Irrgang et al., 2021). GCMs typically represent atmospheric processes with a horizontal grid spacing of about 50-100 km. However, at this coarse resolution,

small-scale processes, such as those associated with clouds, cannot often be explicitly resolved. These complex subgrid scale processes interact with the resolved model scales only through parameterizations tuned in a way to improve the agreement with theory or observations (Hourdin et al., 2017). Parameterization schemes are a necessary but non-trivial part of climate modeling, introducing uncertainties in future climate projections. These uncertainties frequently result in persistent model biases, especially over climatically sensitive regions of the world, such as the Arctic (Sledd & L'Ecuyer, 2021; Tan & Storelvmo, 2019) and the Southern Ocean (Schuddeboom & McDonald, 2021; Vergara-Temprado et al., 2018).

Machine learning (ML)-based parameterizations are a promising and computationally efficient approach increasingly used in climate science to replace, supplement or speed up conventional parameterizations (e.g., Brenowitz & Bretherton, 2019; Gentine et al., 2018; Grundner et al., 2022; Han et al., 2020; Mooers et al., 2021). ML parameterizations are sometimes developed based on high-resolution three-dimensional (3D) simulations, in which subgrid processes are either explicitly resolved (Brenowitz & Bretherton, 2018; Yuval et al., 2021; Yuval & O'Gorman, 2020) or parameterized using conventional schemes (Grundner et al., 2022; O'Gorman & Dwyer, 2018). In this approach, high-resolution data is often coarse-grained to match the lower spatial resolution of the GCM grid (e.g., Brenowitz & Bretherton, 2019). Advances in both computational tools and data assimilation methods have now allowed for global observations to be integrated into ML training datasets (Schneider et al., 2017), yet limitations concerning the limited spatiotemporal coverage of observational data still need to be addressed (Irrgang et al., 2021).

Neural networks (NNs) and random forests (RFs) are two ML methods that have been used for developing parameterizations for GCMs. RF – an ensemble learning algorithm consisting of multiple decision trees – ensures the preservation of physical properties by taking the average predictions of subsets of the training samples (Breiman, 2001). This conservative behavior leads to more stable simulations when coupled with GCMs compared to NNs (Han et al., 2020; O'Gorman & Dwyer, 2018), which can deviate from the training data pool. Notably, RF parameterizations have demonstrated successful emulation of conventional convective schemes in GCMs (O'Gorman & Dwyer, 2018). Yuval and O'Gorman (2020) applied RF parameterization using coarse-grained, high-resolution outputs from an idealized simulation, achieving effective replication of climate patterns across different grid spacings. In contrast, NN parameterizations, although requiring less memory in GCMs, can introduce numerical instabilities and result in model runaway or climate drift (Rasp et al., 2018; Brenowitz & Bretherton, 2018, 2019). To ensure stable long-term simulations, post-prediction adjustments and accurate processing of the training dataset are necessary (Rasp, 2020; Yuval et al., 2021). While offline comparisons favored NN parameterizations, both RF and NN algorithms satisfied physical constraints (energy conservation and non-negative surface precipitation) and demonstrated comparable performance when coupled with the dynamical core of a coarse-resolution aqua-planet GCM (Yuval et al., 2021). Additionally, RFs and NNs showed similar performance in predicting the probability density function of surface solar irradiance under 3D cumulus clouds (Gristey et al., 2020).

Parameterizations of cloud microphysical processes and aerosol-cloud interactions are perhaps one of the most challenging aspects of climate simulations (e.g., Liu et al., 2023; Hugh Morrison et al., 2020). They are also computationally expensive because they require a large amount of information to be carried around in simulations (e.g., cloud microphysical and aerosol

quantities and their interactions) and the parameterizations themselves also may require considerable computational effort. Few studies to date try to simplify cloud microphysical processes using ML-based approaches, focusing on warm cloud microphysical processes. For instance, Seifert & Rasp (2020) employed a Monte Carlo superdroplet simulation to train neural network (NN) models for parameterizing autoconversion, accretion, and self-collection rates in two-moment schemes. Chiu et al. (2021) developed NN-based parameterizations for autoconversion and accretion rates, incorporating in-situ observations of droplet size distributions and employing the stochastic collection equation with bin microphysics to separately account for cloud and drizzle water contents. Although these ML approaches were evaluated offline, Gettelman et al. (2021) successfully replaced the computationally expensive bin microphysical scheme used in a GCM with ML emulators to predict autoconversion and accretion tendencies, achieving comparable accuracy with reduced computational costs. However, there remains a research gap regarding ML parameterizations specifically tailored to represent cold cloud microphysics.

This study focuses on developing an RF-based approach for parameterizing secondary ice production (SIP) in stratiform mixed-phase clouds (MPCs) which are prevalent in polar regions (de Boer et al., 2009; Shupe et al., 2006), sustained by a complex interplay of microphysics, dynamics, radiatively-driven turbulence, as well as surface heat and moisture fluxes (Morrison et al., 2012). Misrepresentation of the mid- and high-latitude MPCs in GCMs has been shown to increase the spread of predicted cloud feedbacks in the recent Climate Model Intercomparison Project (phase 6 – CMIP6; Murray et al., 2021; Zelinka et al., 2020). Furthermore, the ice and liquid phase partitioning in GCMs can significantly impact Arctic amplification, highlighting the necessity of revisiting the microphysical parameterizations associated with Arctic MPCs (Tan & Storelvmo, 2019).

Ice multiplication, also known as SIP, can be an important source of ice particles in MPCs, as it can rapidly increase the pre-existing ice crystal number concentrations (ICNCs) through a number of collisional processes (Field et al., 2017; Korolev & Leisner, 2020). The most frequently acknowledged SIP mechanism is the Hallett-Mossop (HM; Choularton et al., 1980; Hallett & Mossop, 1974), ice-ice collisional break-up (BR; Takahashi et al., 1995; Vardiman, 1978) and droplet-shattering (DS; Choularton et al., 1980; James et al., 2021; Kleinheins et al., 2021). Observations of MPCs in the Arctic region have shown high concentration of ICNCs that greatly surpass ice nucleating particle (INP) concentrations (Wex et al., 2019), particularly at temperatures above -25 ˚C (Luke et al., 2021; Pasquier et al., 2022; Rangno & Hobbs, 2001; Schwarzenboeck et al., 2009). This suggests that SIP must be a prevalent process in the moderately cold polar conditions.

Along with observations, modeling studies across scales have also emphasized the significance of incorporating SIP parameterizations in regional and global climate model simulations for an accurate representation of the phase partitioning and radiative properties of Arctic MPCs (e.g., Fridlind & Ackerman, 2019; Sotiropoulou et al. 2020; 2021; Zhao et al. 2021; Zhao and Liu 2021; 2022). Recent physically-based SIP parameterizations tested in GCMs were developed by pooling experimental observations and further considering the physics of collisions or applying correction factors to account for the simplified laboratory setups (Phillips et al., 2017; 2018). These advanced SIP formulations require that the host model explicitly describes a number of ice (cloud ice, snow and graupel) and liquid species (cloud droplets and raindrops) as well as interactions among them (i.e., aggregation, collection and riming). Zhao et al. (2021) and

Zhao & Liu (2022) developed a hybrid-bin framework for improved representation of SIP, but this approach can be computationally expensive (Sotiropoulou et al., 2022).

Here we propose a new approach towards parameterizing SIP in stratiform MPCs, which we call the RaFSIP (Random Forest SIP) parameterization. RaFSIP is derived from comprehensive model output from mesoscale model simulations that account for all three SIP processes: HM, BR and DS. Following this, the effect of SIP is expressed either directly by predicting the corresponding SIP rates or through the use of the ice-enhancement factor (IEF), which is a multiplication factor applied to primary ice crystals. To account for the effects of SIP for a wide range of stratiform conditions, the RaFSIP parameterization is trained using key thermodynamic and microphysical variables to facilitate its implementation in most models with double-moment representations of ice hydrometeors.

2 Data and Methods

The reference simulation used to develop the RF framework is derived from the mesoscale Weather Research and Forecasting (WRF) model. The WRF outputs from the target simulation were used to train two different versions of the RaFSIP parameterization: the first version of the parameterization predicts the effect of SIP through the use of a multiplication factor applied to the primary ice production rates (hereafter denoted as RaFSIPv1), while the second version is trained to predict directly the production rates of secondarily formed ice particles (hereafter referred to as RaFSIPv2). The workflow followed to develop each parameterization is summarized in Figure 1.

2.1 WRF regional climate simulations

The target simulation was generated using WRF version 4.0.1, including augmented cloud microphysics that considers the effects of BR and DS mechanisms introduced by Sotiropoulou, Vignon, et al. (2021) and Georgakaki et al. (2022), in addition to the default HM parameterization. A regional climate configuration was employed (Abdelwares et al., 2018), where a 50-km resolution parent domain covering the Arctic region contains a single-way nested domain of 10-km resolution. Figure 1 shows the map of the two domains centered over Ny-Ålesund using a polar-stereographic projection, that is suitable for high-latitude WRF domains. The outermost domain consists of 148×148 grid points, while the innermost one contains 301×301 grids. In the hybrid terrain-following mass coordinate system adopted by WRF, we used 40 vertical levels up to a model top of 50 hPa (i.e., ~20 km), with the standard grid spacing generated automatically by WRF.

The initial and lateral boundary conditions are taken from the fifth generation of the European Centre for Medium-Range Weather Forecasts (ECMWF) atmospheric reanalyses dataset (ERA5; Hersbach et al., 2020), with a 31-km horizontal grid spacing. The lateral forcing at the edge of the parent domain was updated every 6 h. To ensure realistic synoptic dynamics in the model and allow for a comparison between in situ observations and simulations, the outer domain of WRF has been nudged toward ERA5 reanalysis for zonal and meridional wind speed, with a relaxation time scale of 6 h. Static fields come from default WRF pre-processing system datasets with a resolution of 30'' for both the topography and land use fields. The WRF physics options include the Rapid Radiative Transfer Model for General Circulation Models (RRTMG) radiation scheme to parameterize both the shortwave and longwave spectra, the local Mellor-

Yamada-Nakanishi-Niino Level 2.5 (MYNN; Nakanishi & Niino, 2006) scheme with its associated surface layer scheme for the planetary boundary layer (PBL) processes representation, the Noah land surface model (Noah LSM; Chen & Dudhia, 2001) for surface options, and the Kain–Fritsch cumulus parameterization, which was activated in both domains.

Cloud microphysics is treated using the scheme of Morrison et al. (2005) (hereafter M05), which represents raindrops, cloud ice, snow and graupel particles with a double-moment approach. However, a single-moment approach is used for cloud droplets, which requires predefining a constant number concentration. For this study, we assumed that an average cloud droplet number concentration of 100 cm^{-3} is suitable for Arctic clouds (e.g., McCoy et al., 2020; Young et al., 2016). Regarding ice formation processes, M05 includes parameterizations for homogeneous freezing at temperatures below -40 ˚C, as well as heterogeneous ice nucleation initiated below -4 ˚C. The latter accounts for immersion freezing of cloud droplets and raindrops (Bigg, 1953), contact freezing (Meyers et al., 1992) and condensation/deposition freezing nucleation (Cooper, 1986), all of which are dependent only on temperature.

In the standard M05 code there is only one SIP mechanism described – the HM process – which is activated after cloud droplets or raindrops rime onto snow or graupel particles within a specific temperature range between -8 and -3 ˚C (Cotton et al., 1986). The activation of this process depends on preset thresholds concerning the minimum mass mixing ratios of the involved ice and liquid species that are found to limit its efficiency and were removed (Atlas et al., 2020; Karalis et al., 2022; Young et al., 2019).

A detailed description of the BR implementation in M05 is provided in Sotiropoulou, Vignon, et al. (2021). The default M05 code was updated to include all possible collisional interactions among the three ice hydrometeor species (see their Appendix B). The number of fragments produced is parameterized as a function of the ice particle size, habit, degree of riming as well as the collisional kinetic energy, following Phillips et al. (2017). Two types of collisions were considered: those involving only high-density precipitating ice particles (such as graupel), and those involving collisions of rimed snow or cloud ice particles with any ice species. The rimed fraction and ice habit were used only in the formulation describing the latter type of collisions, but they were not explicitly resolved in the M05 scheme. BR was enabled only when there was a nonzero rimed mass of either raindrop or cloud droplet onto the ice particle that would undergo fragmentation. A rimed fraction of 0.4 was prescribed, based on previous studies that showed better agreement with observations in polar clouds (Sotiropoulou et al., 2020; Sotiropoulou, Vignon, et al., 2021). Regarding the ice habit, we assumed planar ice particles, as they capture a wider range of conditions in terms of temperature and particle shapes compared to dendritic ice crystals. Sotiropoulou, Ickes, et al. (2021) suggested that the absence of a thorough handling of ice habit and rimed fraction in most bulk microphysics schemes does not seem to significantly impact the depiction of BR in polar conditions. All secondary ice fragments produced by the BR mechanism are added to the cloud ice category.

Georgakaki et al. (2022) described the implementation of the DS mechanism in the M05 scheme of WRF. We considered two collision modes that can cause the freezing and subsequent shattering of large raindrops, as described by Phillips et al. (2018). The first mode, or 'mode 1', occurs when a supercooled raindrop collides with a less massive cloud ice particle or when an INP initiates freezing in immersion mode. Freezing probability is set to unity and zero for temperatures below -6°C and above -3°C, respectively, with intermediate values in between. The shattering probability depends on raindrop size, being 0 for sizes smaller than 50 μm, 1 for sizes

larger than 60 μm, and varying for sizes in between. The second mode, or 'mode 2', involves collisions between raindrops and larger ice particles such as snow or graupel (James et al., 2021), producing only tiny ice fragments that are passed to the cloud ice category. Big fragments are treated as either graupel, snow, or frozen drop depending on the type of collision that initiated the raindrop freezing process.

The regional climate set-up (Figure 1) with augmented cloud microphysics was employed to run a reference WRF simulation for two years from 2016 to 2017, preceded by a 1-week spin-up period starting on December 25, 2015. This time frame was considered sufficient to capture the possible parameter space in the atmospheric state. High-resolution three-dimensional snapshots of the simulation with a 10-km resolution domain (the area bounded by the dashed lines in Figure 1), were saved every 3 h. These snapshots formed the basis for developing the ML parameterization, which will be described in the following section.

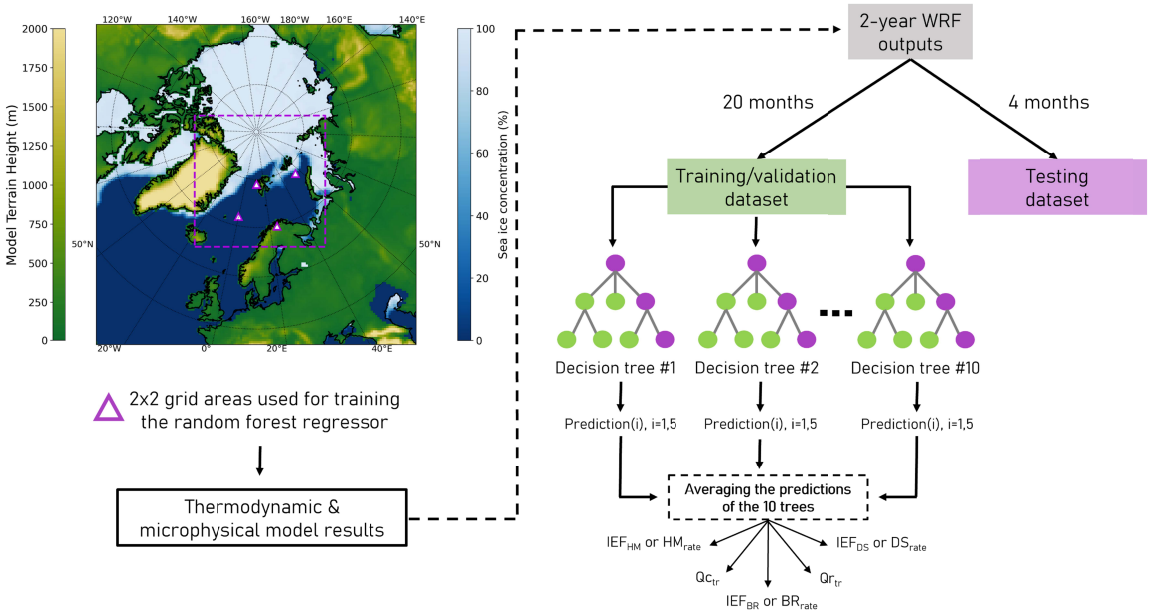

Figure 1. Schematic diagram of the methodology followed to develop the two versions of the RaFSIP parameterization. The map on the left shows the two WRF domains used to simulate the two-year period required for training the RaFSIP parameterization. The rectangular region marked by the purple dashed lines delimit the 10-km resolution domain, while colors indicate terrain heights (left axis) and sea ice concentration (right axis). The 4 triangles represent the regions from where the training dataset is extracted. The two-year high-resolution model output is split into ~85% training dataset (20 months) and ~15% testing dataset (4 months). The RaFSIPv1 (RaFSIPv2) parameterization is trained to predict the IEF (SIP_{rate}) as well as the transfer of mass from cloud droplets (Qc_{tr}) or raindrops (Qr_{tr}) to cloud ice due to SIP. The snapshot corresponds to the monthly average of January, 2016.

2.2 Random forest (RaFSIP) parameterization development

RaFSIP is based on a random forest regressor (RFR) algorithm, which is a supervised ML technique, consisting of an ensemble of decision trees (Breiman, 2001) trained directly from

the outputs of the high-resolution WRF simulation. To minimize variance, each decision tree is trained on a random subset of the training data and a random subset of the inputs – also called as features – of that data. The RFR prediction is calculated by averaging over the individual decision trees, which reduces the risk of overfitting and improves generalization performance compared to a single decision tree. RFR can capture non-linear relationships between input features and output variables and is proficient at interpolation. However, it cannot extrapolate due to its predictions being averages over subsamples of the training dataset. This helps ensure that a RF-based parameterization will be robust when coupled with a model in an online setting, such as in our case.

2.2.1 Description of the two parameterization approaches

Depending on the prevailing temperature and the presence of rime onto ice particles, we expect different SIP processes to be activated. This is the reason why the two versions of the RaFSIP parameterization consist of a number of RFR models, each one of them being responsible for predicting the effect of SIP as dictated by the thermodynamic and microphysical state describing every model timestep. The RFR models consisting the RaFSIPv1 parameterization, are trained to predict the so-called IEF, which is the ratio between the production rate of secondary ice particles from each SIP process (HM_{rate}, BR_{rate} and DS_{rate}), and primary ice particles via heterogeneous freezing of cloud droplets (PIP_{rate}). Hence, RaFSIPv1 provides 3 predictions: IEF_{HM}, IEF_{BR}, and IEF_{DS}, the contribution of which can be added to yield the total IEF: $\mathrm{IEF} = SIP_{rate}/PIP_{rate}$. The notation of IEF is frequently employed in the literature as an indication of the prevalence of SIP, in both observational (e.g., Korolev et al., 2022; Wieder et al., 2022) and modeling studies (e.g., Waman et al., 2022; Zhao et al., 2023).

In RaFSIPv2, the RFR models predict directly the three SIP rates – HM_{rate}, BR_{rate} and DS_{rate} (in $kg^{-1}\ s^{-1}$), derived from the high-resolution WRF results. The three rates are combined to determine the total SIP_{rate}. As the HM and DS processes move mass from the liquid to the ice species when active (albeit from the rimed liquid particles in the former case), both versions of the RaFSIP parameterization are trained to predict Qc_{tr} and Qr_{tr} (in $kg\ kg^{-1}\ s^{-1}$) corresponding to the mass transferred from the cloud droplets and raindrops to the cloud ice category, respectively. Therefore, the two versions of the RaFSIP parameterization can provide up to five different predictions, given certain SIP conditions are met.

Here, we consider two main temperature regimes: $-8 \leq T < -3$ °C (HM zone) and $-25 \leq T < -8$ °C, which is essential as the HM mechanism can only be effective within the former one. By combining these temperature ranges with the presence or absence of mass production rate of raindrops collected by ice particles (RIMR in $kg\ kg^{-1}\ s^{-1}$), we obtain 4 different RFR models that are used in both versions of the RaFSIP parameterization (Table 1 and 2). Two models can be activated in the HM zone, namely “forestALL” and “forestBRHM”, that are replaced by the “forestBRDS” and “forestBR” at lower temperatures (the suffix of the model name denotes the SIP processes in action). The final selection of which forest to use in the corresponding temperature range is based on the presence of a nonzero RIMR at the current timestep, which is the criterion used to identify the cases where DS might be taking place. The two forests that take into account the effect of DS are the forestALL and forestBRDS models.

Both RaFSIP parameterizations incorporate SIP through BR and DS at temperatures as low as -25°C, which is supported by recent observational findings (Korolev et al., 2022; Pasquier

et al., 2022; Wieder et al., 2022). Approaching warmer subzero temperatures (T > -4 °C), RaFSIPv1 does not predict ice enhancement, since heterogeneous freezing of cloud droplets (i.e., the denominator in the IEF expression) does not occur in the M05 scheme (Section 2.1). In contrast, RaFSIPv2 can still account for the effect of SIP as it is not directly linked to the PIP_{rate}. An additional RFR model called "forestBRwarm" is therefore used in RaFSIPv2 (Table 2), to calculate the BR_{rate} at temperatures between $-3 \leq T \leq 0$ °C. At these warm subzero temperatures, DS is also proposed to contribute to SIP through recirculation (Korolev et al., 2020), but only in tropical or midlatitude frontal systems (Lauber et al., 2021) owing to strong convective turbulent updrafts that are rare in polar stratiform clouds. Therefore, RaFSIPv2 considers that only the BR mechanism initiated by collisions of seeding rimed ice particles can be efficient at temperatures above -3 °C.

2.2.2 Features and training dataset

Both versions of the RaFSIP parameterization share the same input features. The ambient temperature (T in K), total ice water content (IWC in kg kg^{-1}), liquid water content (LWC in kg kg^{-1}), relative humidity with respect to ice (RHi) and mass production rate of cloud droplets rimed onto ice particles (RIMC in kg kg^{-1} s^{-1}) are among the features that have been used in all RFR models of the two versions of the parameterization. Since DS requires the presence of large raindrops, RIMR is also used as input to the models accounting for its effect (i.e., forestALL and forestBRDS). With these 6 inputs we seek to effectively capture all range of cloud states that can initiate and drive ice multiplication. The training dataset was constrained to scenarios with substantial liquid water content (LWC>10^{-5} gm^{-3}), accompanied by nonzero riming tendencies, to ensure the effectiveness of SIP. The 6 inputs are chosen in a way to simplify the detailed SIP formulations (e.g., Phillips et al., 2017; 2018), yet are expected to generate complex mappings for training the RFR models. Here we use the instantaneous predictions of the model for all individual vertical grid cells as inputs for all RFRs, rather than their vertical profiles (e.g., O'Gorman & Dwyer, 2018; Yuval & O'Gorman, 2020).

We generated the training dataset for all RFR models using the 3-hourly high-resolution WRF results (Section 2.1), extracted from 2×2 grid cell regions (16 grid cells in total) indicated by purple triangles in Figure 1. Half of these grid cells represented continental conditions, while the other half were over the sea. The absence of a latitudinal preference in SIP rates between the Northern and Southern hemispheres (Zhao & Liu, 2021) suggests that a limited number of grid points from the 2-year high-resolution simulation of WRF is adequate for capturing the thermodynamic and microphysical conditions associated with SIP events in stratiform conditions. Note that horizontal and vertical coarse-graining is frequently applied when developing ML parameterizations for GCMs based on high-resolution simulations (e.g., Brenowitz & Bretherton, 2019; Grundner et al., 2022; Yuval & O'Gorman, 2020). Indeed, the impact of SIP can vary depending on the scale considered, with higher-resolution simulations exhibiting greater SIP tendencies due to their ability to capture localized and enhanced SIP events. Our goal is to investigate whether a SIP parameterization derived from a 10-km resolution grid (innermost WRF domain) is effective at the coarser resolution of 50-km in the parent domain of WRF, which is closer to the resolutions seen in GCMs. Given that the input tendencies predicted by the coarser-resolution grids will be lower than the higher-resolution ones, we expect that the resulting SIP tendencies will also be smoothed out. An important aspect to consider also here is that the RFR models tend to underestimate extreme values and

359 overestimate low values (Zhang & Lu, 2012). This behavior arises from the fact that RFR
360 predictions are derived as averages of the predictions made by all decision trees within the
361 ensemble.

362 To prepare for training, each feature and output variable is normalized using the natural
363 logarithm, which is important given the range of several orders of magnitude they span (Figure
364 2). During the training process, we excluded IEF values below 10^{-1} and SIP rates below 10^{-5} kg^{-1}s^{-1}
365 (Figure 2). This was made because such values would not result in significant SIP, and we
366 aimed to reduce the range of predictions. The training dataset comprises 20 months of high-
367 resolution WRF results, representing approximately 85% of the data. The remaining 15% of the
368 data, consisting of 4 months (January, April, July, and October 2017), were used for testing the
369 offline performance of the RaFSIP parameterization (Section 3). The RandomForestRegressor
370 class from the scikit-learn package version 1.2.0 (Pedregosa et al., 2011) was used to train each
371 RFR model. All RFR models consisting the two RaFSIP parameterizations were stored as ASCII
372 files.
373

374 2.2.3 Choice of hyperparameters

375 To improve the performance of the RFR models, different hyperparameters governing the
376 learning process can be tuned. The Mean Squared Error (MSE) resulting from the RFR
377 predictions was evaluated using 10-fold cross validation on the training dataset. We selected the
378 number of trees in each forest, the minimum samples per leaf node, and the number of training
379 samples as the three most important hyperparameters to tune. Figure S1 shows the validation
380 curves for the forestALL model (used in RaFSIPv2), which illustrate how the performance of the
381 model varies with different hyperparameter values. The final decision on hyperparameters
382 involves a trade-off between model complexity and runtime, with the latter being crucial for
383 optimizing online performance when coupled with the WRF model. We chose 10 trees in each
384 RFR, a minimum of 4 samples per leaf node, and 25,000 training samples for all RFR models, as
385 these produced comparable validation curves. Note that, for online applications of the RFR
386 models, it is common practice to use 10 decision trees to ensure computational efficiency
387 (O'Gorman & Dwyer, 2018; Yuval & O'Gorman, 2020). The offline performance of the RaFSIP
388 parameterizations will be discussed in Section 3, followed by the online performance in Section
389 4.
390

391 2.3 Implementation of RaFSIP parameterization in WRF

392 To implement the RaFSIP parameterization in WRF, a Fortran 90 module is developed to
393 read and store the parameters for building the RFR models. The ASCII files are only read during
394 the first model timestep and all forest parameters are passed as public variables into the
395 microphysics code. Within the M05 microphysics routine, the RaFSIP parameterization replaces
396 the three detailed inline SIP parameterizations (Section 2.1), taking the fields of T, RHi, LWC,
397 IWC as well as RIMC and RIMR as inputs to make predictions. Calculations for LWC and IWC,
398 consider contributions from all liquid (cloud droplet and raindrops) and ice (cloud ice, snow and
399 graupel) species. RIMC and RIMR encompass all possible ways in which cloud droplets or
400 raindrops are collected by frozen particles in the M05 scheme: (i) droplet/raindrop-cloud ice, (ii)
401 droplet/raindrop-snow, and (iii) droplet/raindrop-graupel. At each model timestep and grid cell,

if certain requirements are met (discussed in Section 2.2.1), a different RFR model may be activated to represent the effect of single or combined SIP processes.

At the end of each model timestep, the RaFSIP parameterization calculates the total SIP_{rate} (in kg^{-1} s^{-1}) either directly or through the use of the IEF, depending on the chosen version. In RaFSIPv1, the SIP_{rate} is obtained by multiplying the number tendency of heterogeneously frozen cloud droplets (in kg^{-1} s^{-1}) by the total IEF. However, this approach has a significant caveat: SIP cannot be accounted for unless a nonzero PIP_{rate} is predicted by the model. Therefore, RaFSIPv1 can only be used at temperatures colder than -4 °C, where PIP is initiated in the model. To ensure that the final SIP_{rate} does not exceed a certain threshold, an upper limit of 100 particles kg^{-1} s^{-1} was applied, corresponding to the highest simulated value in the training dataset. Although our results were not sensitive to the choice of this upper limit, it may be an important consideration for the implementation of RaFSIPv1 in other microphysical schemes employed by different models. The SIP_{rate} predicted by RaFSIPv1 is then added to the cloud ice number concentration conservation equation. The RaFSIPv2 parameterization follows a similar approach to RaFSIPv1, but does not link SIP_{rate} to the instantaneous PIP_{rate}. This direct prediction is enabled by the RFR models, allowing for RaFSIPv2 to be applicable over a wider temperature range from 0 °C to -25 °C, without requiring a nonzero PIP_{rate}.

When HM and/or DS mechanisms are active, the transported masses Qc_{tr} and Qr_{tr} are subtracted from their respective cloud categories and added to the conservation equation for cloud ice mass mixing ratio. It is important to note that the transferred liquid masses involved in SIP were initially part of the rimed masses constituting the RIMC and RIMR quantities. Without SIP, these masses would have been transported to the mass conservation equation of the corresponding rimed ice particles. To avoid double-counting the transferred masses of liquid water, Qc_{tr} and Qr_{tr} should also be removed from the riming tendencies of the involved ice species. To account for this, we subtract the transferred masses from the term with the biggest contribution; given that the terms participating in RIMC and RIMR can vary by several orders of magnitude, this approach ensures that the simulations will not be subject to significant bias.

To evaluate the online performance of the new RaFSIP parameterizations when coupled with the WRF model, we conducted a one-year simulation using the same set-up depicted in Figure 1 (Section 2.1). This simulation covers the period between September 2019 and August 2020, which is more than 1.5 years after the training period, with one additional week of spin-up starting from August 25, 2019. The testing simulation was conducted three times. First, we carried out the ”CONTROL” simulation, which does not take into account any SIP process. Then, we performed the “ALLSIP” simulation, which includes all the detailed inline parameterizations of SIP outlined in Section 2.1. Finally, the “RaFSIP” simulation refers to the one where the RaFSIP parameterizations replaced the detailed SIP descriptions. By comparing the results of the ALLSIP simulation with those of the RaFSIP simulation in Section 4, we seek to examine the robustness of the new SIP parameterizations in terms of computational efficiency and result quality.

3 Offline performance of RaFSIP parameterizations and feature importance

To evaluate the performance of both RaFSIP parameterizations, each RFR model was tested on the 4-month dataset that was not used during training (Section 2.2.2). The performance was assessed using two metrics summarized in Tables 1 and 2: Root-Mean-Square Error

(RMSE) and coefficient of determination (R^2), which were calculated based on the normalized output variables. R^2 is defined as one minus the ratio of the sum of squared errors to the true variance. The offline performance of the forestALL model, which is used by both RaFSIP parameterizations when all conditions for SIP processes are met, is shown in Figure 2. For the rest of the RFR models, the offline performance is displayed in Figures S2 to S5, in the Supporting Information.

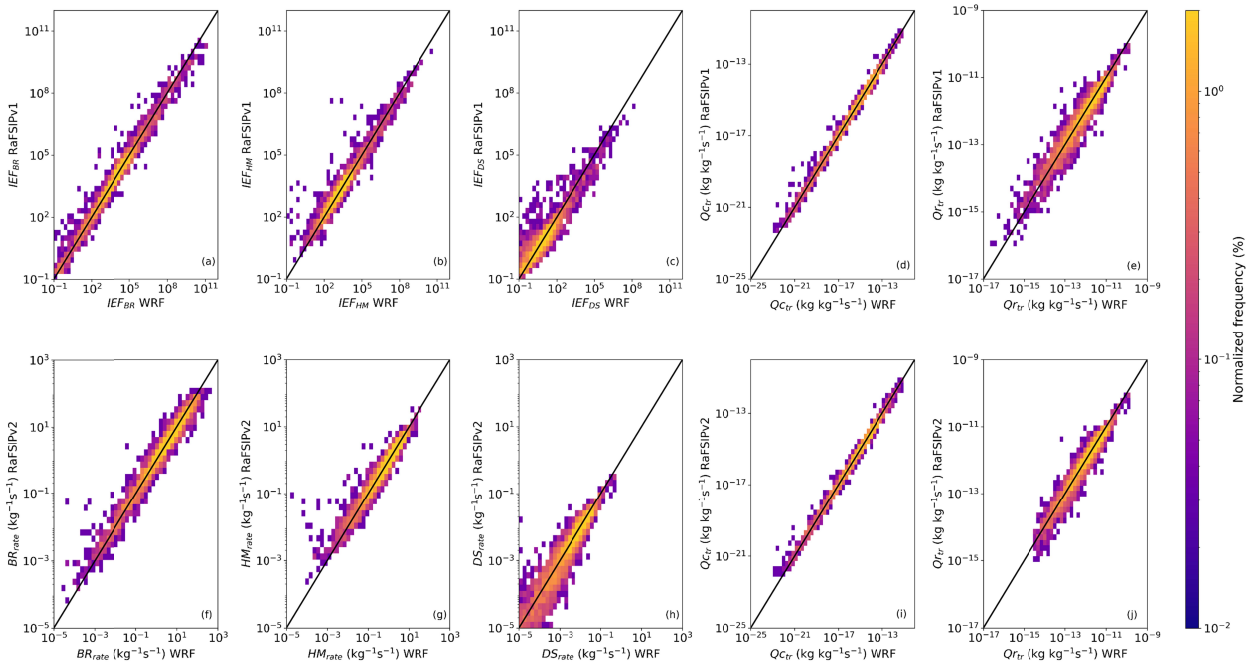

Figure 2. Normalized histograms (i.e., frequency is scaled by the total number of predictions) of the true WRF results versus the forestALL predictions used in (top panel) RaFSIPv1 parameterization to predict the IEF due to (a) BR, (b) HM, (c) DS, and the transferred masses from (d) cloud droplets (Qc_{tr}) and (e) raindrops (Qr_{tr}) to cloud ice, and (bottom panel) RaFSIPv2 parameterization to predict the SIP rate due to (f) BR, (g) HM, (h) DS, and the transferred masses (i) Qc_{tr} and (j) Qr_{tr}. The black line represents the one-to-one line.

All five outputs of the forestALL model present a wide range of values (Figure 2), making accurate prediction challenging. For instance, IEF_{BR} and IEF_{HM} vary from 10^{-1} to 10^{11}, while IEF_{DS} is confined below $\sim 10^{8}$, with predictions more spread out along the 1:1 line, especially at lower values. The RaFSIPv1 parameterization predicts an inverse relationship between IEF and PIP_{rate} (not shown), primarily due to the PIP_{rate} being in the denominator of the IEF expression. The competing relationship between SIP and PIP has also been highlighted in previous modeling studies (e.g., Georgakaki et al., 2022; Zhao & Liu, 2022), as an outcome of the enhanced ice nucleation leading to more glaciated MPCs with fewer precipitating particles such as rain or graupel. Note that the predicted IEF values are higher than those frequently reported in the literature (e.g., Waman et al., 2022; Zhao et al., 2023), as they are extracted from the ratio of tendencies rather than integrated particle concentrations. Similar trends are observed in the SIP rates predicted by RaFSIPv2 (Figure 2f, g, h), with the BR and HM processes again proving more efficient at producing SIP particles compared to DS.

Although RaFSIPv1 and RaFSIPv2 use the same predictors, the former is limited to cases where PIP_{rate} is nonzero, resulting in noticeable differences among the two approaches. To evaluate the relevance of each input feature in the predictions made by the RFR models, we employed the permutation importance metric (Figure S6 to S10) from the RandomForestRegressor class of scikit-learn. This metric estimates feature importance by randomly permuting its values and measuring the consequent decrease in model performance. This approach can capture the effect of both linear and nonlinear relationships between features and target variables, and can also help identify any potential overfitting issues in the RFR models. Note that here we used the negative RMSE as the scoring parameter and normalized the resulting variable importance by dividing by the maximum value among features.

The most significant features in the predictions made by all RFR models are the riming tendencies and the IWC. Specifically, inside the HM zone, RIMC has the highest permutation importance score for the forestALL (Figure S6) and forestBRHM (Figure S7) models employed in both RaFSIP versions. The two mass tendencies, RIMC and RIMR, are explicitly used as inputs in the detailed parameterized expression of HM in the default M05 scheme (Section 2.1). Outside the HM zone, where BR can lead to larger IEF or SIP_{rate} compared to DS, IWC becomes the more important feature for the predictions of the RFR models, particularly for forestBR (Figure S9) and forestBRwarm (Figure S10), with the amount of (rimed) cloud droplets becoming the second most important feature. The increase in IWC, associated with ice sedimenting from higher-level clouds, is frequently found to drive the BR process (Georgakaki et al., 2022; Järvinen et al., 2022; Pasquier et al., 2022; Ramelli et al., 2021; Sotiropoulou, Vignon, et al., 2021).

Table 1.
Root-Mean-Square Error (RMSE) of the output variables predicted by the RaFSIPv1 parameterization, along with the corresponding coefficient of determination (R^2) values in parentheses.

RaFSIPv1	**Conditions**		**Predictions**				
model	Temperature	RIMR	IEF_{BR}	IEF_{HM}	IEF_{DS}	Qc_{tr}	Qr_{tr}
forestALL	-8≤T<-3˚C	>0	0.32 (0.97)	0.36 (0.94)	0.46 (0.86)	0.17 (0.99)	0.26 (0.93)
forestBRHM	-8≤T<-3˚C	=0	0.37 (0.98)	0.12 (0.98)	–	0.09 (0.99)	–
forestBRDS	-25≤T<-8˚C	>0	0.31 (0.97)	–	0.38 (0.87)	–	0.39 (0.83)
forestBR	-25≤T<-8˚C	=0	0.44 (0.97)	–	–	–	–

Using the different RFR models depending on the prevailing thermodynamic and microphysical conditions allowed us to evaluate the performance of the RaFSIP parameterizations under various scenarios. The distribution of all RFR predictions against true values, as shown in Figure 2 and Figures S2 to S5, indicates that predictions with a higher relative frequency of occurrence are closer to the 1:1 line for both RaFSIP approaches. The

statistical metrics presented in Tables 1 and 2 can differ significantly depending on the prevailing conditions and the SIP processes involved. The RMSE for RaFSIPv1 predictions varied from ~10-45%, while for RaFSIPv2, it ranged between ~15-40%. The transferred masses due to SIP, Qc_{tr} and Qr_{tr}, are generally well-predicted in most of the RFR models with an RMSE of less than 30%, despite spanning more than 10 orders of magnitude.

In cases where multiple SIP processes are present, the prediction error tends to be higher for DS, as shown in Figures 2c and 2h and reflected in the higher RMSE values in Tables 1 and 2. To improve the offline accuracy of the forestALL and forestBRDS models for predicting this SIP mechanism, we tested the inclusion of the size of raindrops undergoing DS as a potentially important predictor. The resulting RMSE metrics showed a ~5% decrease in the forestBRDS model, while the forestALL model remained unaffected (not shown). However, since the total effect of SIP is cumulative and DS is the least significant mechanism compared to the other two, any errors associated with its uncertain representation are not likely to significantly impact the online performance of the RaFSIP parameterizations. Therefore, we argue that adding more predictors may not be worth the increased model complexity.

Table 2.
Root-Mean-Square Error (RMSE) of the output variables predicted by the RaFSIPv2 parameterization, along with the corresponding coefficient of determination (R^2) values in parentheses.

RaFSIPv2 model	Conditions		Predictions				
	Temperature	RIMR	IEF_{BR}	IEF_{HM}	IEF_{DS}	Qc_{tr}	Qr_{tr}
forestALL	-8≤T<-3˚C	>0	0.23 (0.96)	0.22 (0.93)	0.36 (0.87)	0.16 (0.99)	0.21 (0.94)
forestBRHM	-8≤T<-3˚C	=0	0.34 (0.96)	0.36 (0.90)	–	0.18 (0.99)	–
forestBRDS	-25≤T<-8˚C	>0	0.17 (0.97)	–	0.27 (0.89)	–	0.27 (0.89)
forestBR	-25≤T<-8˚C	=0	0.28 (0.96)	–	–	–	–
forestBRwarm	0≤T≤-3˚C	=0	0.38 (0.96)	–	–	–	–

When only BR is active, either in the colder (i.e., forestBR) or warmer (i.e., forestBRwarm) temperature regime, the RMSE scores range between ~30-45% (Tables 1 and 2). This could indicate and important input feature related to BR may be missing or that the relationship between the input features and the target variable (IEF_{BR} or BR_{rate}) is inherently difficult to model accurately due to the level of non-linearity. In the physically-based parameterization by Phillips et al. (2017), the SIP fragments generated after BR depend on collisional kinetic energy, which is an uncertain parameter as it is a function of the difference in terminal velocities of colliding ice particles. The latter follows a fall-speed-diameter relationship, the parameters of which are highly uncertain and can directly impact both the precipitation rates and the SIP efficiency (Karalis et al., 2022). Therefore, we chose not to include collisional kinetic energy in our set of predictors, as it would increase model complexity without necessarily

improving accuracy. The predictors we chose strike a good balance between model complexity and accuracy, allowing us to describe SIP occurrence as a function of simplified inputs that most GCMs can predict.

4 Coupling the RaFSIP parameterization with WRF

In this section, we aim to assess the performance of the parameterization when coupled back with the dynamical core of the WRF model, making fast and precise predictions at runtime. To facilitate the discussion, in the rest of the paper we will focus on the results of the RaFSIPv2 parameterization, while the corresponding RaFSIPv1 results will be available in the Supporting Information. RaFSIPv2 can predict SIP rates directly, making it less coupled with the WRF model on which it was trained. In contrast, the approach followed in RaFSIPv1 tends to be more dependent on the PIP rates predicted by each model, implying that its good online performance in WRF may not be guaranteed in other models using different PIP schemes.

When introducing the RaFSIP parameterization into the M05 scheme of WRF, two main concerns had to be addressed in order to ensure the robustness of the approach: model stability and computational efficiency. The stability of the model was tested during the one-year test simulation starting from September 2019 until August 2020 (Section 2.1). The coupled WRF model with the RaFSIP parameterization ran stably across a wide range of conditions. Regarding computational efficiency, the new parameterization performed comparably to the inline SIP parameterizations without increasing computational demands. This implies that the RaFSIP scheme can be easily incorporated into existing models without significant impact on runtime, being a result of carefully selecting the number of trees in the RFR models. In the following discussion all results will be divided into four groups according to season.

4.1. Horizontal distribution of ice crystal number concentrations

Latitude-longitude snapshots of the median ICNCs obtained from the instantaneous 3-hourly outputs of the CONTROL, ALLSIP, and RaFSIP experiments (Section 2.3), along with the resulting R^2 between the predictions of the latter two, provide a way to assess the quality of the WRF predictions when coupled with the RaFSIPv2 parameterization (Figure 3). Note that the modeled ICNCs include the contribution of all three ice species (cloud ice, snow and graupel). To calculate the median ICNCs presented in Figure 3 we considered only the in-cloud conditions represented by ICNCs > 10^{-5} L^{-1} and temperatures between -25 and 0 °C, which is the range where RaFSIPv2 can be active. For calculating the median values and R^2 scores, we went through each latitude and longitude reshaping the remaining two dimensions (time and height). To facilitate the identification of patches where RaFSIPv2 performs favorably in terms of R^2, we further coarse-grained the information from the coarse-resolution grid mesh by dividing the original grid into non-overlapping 3×3 sub-grids, and computing the average value of each sub-grid. Thus the R^2 map in Figure 3 is projected onto a 49×49 mesh.

The RaFSIPv2 parameterization coupled with WRF can skillfully predict the median horizontal distribution of ICNCs, closely following the pattern produced by the ALLSIP simulation with the detailed SIP descriptions. Darker blue shades are produced by ALLSIP and RaFSIP indicating the higher median ICNCs compared to CONTROL. The increase in median ICNCs is observed for all four seasons, even though it is more prevalent during winter and spring, particularly in the sea region between Greenland and Canada to the west and extending to

the north of the Scandinavian Peninsula to the east. In these areas the median seasonal ICNCs can exceed 10 L^{-1}, suggesting the significant role of ice multiplication processes in elevating the median ICNCs by up to an order of magnitude when SIP conditions are met.

Despite being trained on a small subset of high-resolution WRF grid cells, the RaFSIPv2 parameterization can generalize and accurately predict the locations of ice enhancement in the coarser resolution domain as dictated by the ALLSIP results. The R^2 maps superimposed in Figure 3 reveal patches of especially high predictive skill denoted with R^2 scores exceeding 90%. The accuracy of the predictions largely exceeds 80% of R^2 over localized areas of significant ice enhancement, shown with darker shades on Figure 3g and 3k. This implies the ability of RaFSIPv2 to reproduce the physical processes occurring in polar MPCs. However, the southeast part of Greenland poses a challenge for accurate model predictions, with R^2 dropping below 60%, especially in winter.

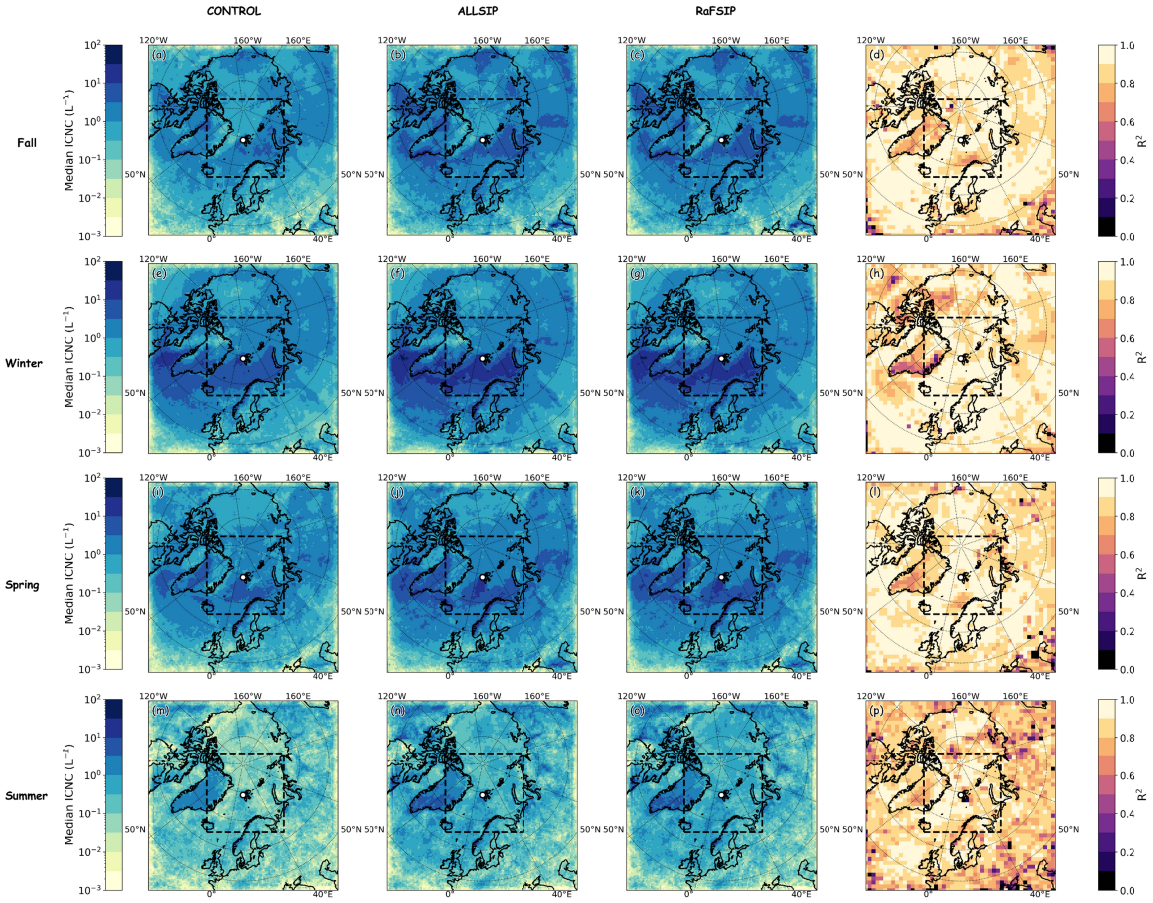

Figure 3. Latitude-longitude maps of the median ICNC simulated by the (a, d, g, j) CONTROL, (b, e, h, k) ALLSIP, and (c, f, i, l) RaFSIP simulations, along with the corresponding (d, h, l, p) R^2 computed between ALLSIP and RaFSIPv2 results. Statistics are calculated for the 4 simulated seasons: fall (top panel), winter (second panel), spring (third panel) and summer (bottom panel).

Compared to other seasons, the predictive skill of RaFSIPv2 is reduced during summer, with R^2 dropping below 40% in very localized regions close to the edges of the WRF domain.

Higher temperatures are not likely the cause of lower R^2 values, as the RaFSIPv2 models were trained using a wide range of temperatures and temperature was not found to be among the most important input features for the predictions of the RFR models (Figures S6-S10). A possible explanation could be that during summer the expected shift towards warmer clouds may lead to increased riming tendencies, which can be associated with higher SIP rates in RaFSIPv2. Replacing the RaFSIPv2 parameterization with the RaFSIPv1 in WRF, results in a further decline in the predictive skill in all four seasons, as shown in Figure S11. The R^2 scores decrease to below 60% in most regions with significant ice enhancement, with a further drop to below 40% during the summer months. The degradation in the performance of the model is most likely because of RaFSIPv1 requiring a nonzero value of PIP_{rate} to provide ice enhancement.

Table 3 presents median statistics extracted from all three sensitivity experiments during the cold (autumn and winter) and warm (spring and summer) seasons. The latitudinal zones north of 70°N are divided into three groups, and the results are grouped into two distinct temperature ranges ($-10 \leq T \leq 0^{\circ}C$ and $-20 \leq T < -10^{\circ}C$) where SIP effects are more prevalent. During the cold season, it is observed that the CONTROL simulation leads to higher median ICNCs in the warmer temperature regions compared to the colder one at latitudes 70-80˚N, which may seem contradictory since PIP efficiency generally increases with decreasing temperatures. This unexpected finding could potentially be explained by ice seeding from colder clouds enhancing the median ICNCs in lower-level warmer clouds at temperatures above -10˚C, or by increased efficiency of ice aggregation leading to significantly lower median ICNCs in the colder temperature range ($-20 \leq T < -10^{\circ}C$) (Barrett et al., 2019; Chellini et al., 2022).

The introduction of SIP in the WRF simulations results in a substantial increase in median ICNCs, particularly in the warmer temperature bin during the cold (warm) season, where ALLSIP and RaFSIP simulations show a factor of approximately 2-3 (3-6) higher ICNCs compared to the CONTROL simulation. On the other hand, in the colder temperature bin, the ICNC enhancement in ALLSIP and RaFSIP is relatively modest, reaching only up to ~20-25% during both examined seasons. It is worth noting that latitudes above 80°N display systematically lower ICNCs, with no significant contribution of SIP being observed at temperatures below -10°C, likely due to complete cloud glaciation. Overall, the median statistics derived from the WRF simulation coupled with the RaFSIPv2 parameterization are in good agreement with the ALLSIP simulation results during the cold and warm seasons examined here (Table 3).

To assess the agreement between our WRF results and satellite remote sensing data, we compare our median values from the 3 sensitivity experiments to the 10-year median values between 2006-2016 presented in (Papakonstantinou-Presvelou et al., 2022). Their study, which focused on low-level pure ice clouds, demonstrated that higher ICNCs are found over sea ice compared to open ocean, a finding contrary to previous expectations. To ensure comparability with Figure 1 of Papakonstantinou-Presvelou et al. (2022), we calculated the median ICNC statistics focusing on grid points over sea ice with a glaciation fraction exceeding 98% and a sea ice concentration higher than 50%. These are annotated as $ICNC_{si}$ in Table 3. The glaciation fraction was determined by calculating the ratio of modeled IWC to total water content (TWC = IWC + LWC).

In the glaciated clouds simulated between -10°C and 0°C, the contribution of SIP is crucial for bringing the modeled $ICNC_{si}$ closer to the 10-year median observed values (Figure 1 in Papakonstantinou-Presvelou et al., 2022). At these warmer subzero temperatures, both

ALLSIP and RaFSIP, enhance the median $ICNC_{si}$ by a factor of up to ~2 compared to the CONTROL simulation of WRF during both seasons (Table 3). Note that glaciated conditions prevent the effect of SIP from manifesting with higher enhancement factors. This is particularly evident at temperatures below -10°C, where the efficiency of ALLSIP and RaFSIP in producing SIP particles diminishes. At these temperatures, all three experiments underestimate the observed median $ICNC_{si}$ levels (which reach up to ~3 or 4 L^{-1}) at all latitudes. The missing ice crystal source in this temperature range may be primarily due to the representation of PIP in the model.

Table 3.
Median ICNC for different latitudinal zones, temperature ranges, and seasons, obtained from three different WRF experiments. The cold season values were extracted from September 2019 to February 2020, while the warm season values were obtained from March to August 2020. The values in all four columns represent the results from the CONTROL/ALLSIP/RaFSIP experiments. The subscript $ICNC_{si}$ indicates that the median ICNC is derived for glaciated clouds (glaciation fraction > 0.98) from model grid points over the sea-ice (sea-ice concentration > 50%).

Latitude	Temperature range (˚C)	Median ICNC cold (L^{-1})	Median ICNC warm (L^{-1})	Median $ICNC_{si}$ cold (L^{-1})	Median $ICNC_{si}$ warm (L^{-1})
70-75°N	[-10,0]	1.9/4.6/4.5	0.2/0.6/0.6	4.0/7.5/7.6	3.2/5.8/5.7
	[-20,-10)	1.5/1.9/1.7	1.2/1.4/1.3	1.4/1.5/1.7	2.5/2.7/2.8
75-80°N	[-10,0]	1.8/4.1/4.2	0.1/0.5/0.6	4.0/6.2/6.5	2.9/5.0/4.9
	[-20,-10)	1.2/1.5/1.4	0.9/1.1/1.1	1.4/1.4/1.5	2.3/2.4/2.5
> 80°N	[-10,0]	0.4/1.1/1.3	0.09/0.3/0.5	2.5/3.8/4.1	2.0/4.2/4.1
	[-20,-10)	0.8/0.9/0.8	0.8/1.0/0.9	1.0/1.1/1.2	1.5/1.6/1.7

4.2. Joint probability distributions of simulated cloud properties

Figure 4 illustrates the bivariate joint probability density function (PDF) of the median ICNCs as a function of temperature and glaciation fraction. This figure aims to provide further insight into the conditions where the RaFSIP parameterization is expected to perform better. The statistics were derived using instantaneous 3-hourly results from the CONTROL, ALLSIP, and RaFSIP sensitivity experiments (Section 2.3), focusing again on the in-cloud conditions characterized by significant concentrations of ice crystals (ICNC > 10^{-5} L^{-1}), as well as ice and liquid masses (IWC, LWC > 10^{-6} gm^{-3}).

4.2.1 Median ice crystal number concentration

Figure 4 reveals that the WRF model, coupled with the RaFSIPv2 parameterization, can accurately capture the most prominent patterns of the median 2D-binned ICNCs in all four seasons compared to the ALLSIP simulation with detailed inline microphysics. This is particularly true for temperatures ranging from -8 to -3 °C and glaciation fraction below ~25-30% or higher than ~80%. The turquoise bands in the lower right of the 2D-binned ICNCs indicate the importance of SIP in relatively warm polar clouds. At these temperatures, supercooled liquid water prevalent in simulated MPCs enhances riming tendencies (RIMC and/or RIMR) and facilitates the action of SIP, resulting in modeled ICNCs up to an order of magnitude higher in the ALLSIP and RaFSIP simulations, compared to the CONTROL simulation. These findings align with the results of Arctic clouds presented by Sotiropoulou et al. (2020), which reported a 10-20 fold increase in ice when both HM and BR were considered, with the effectiveness of BR decreasing in moderately colder clouds (Sotiropoulou, Ickes, et al., 2021).

At higher glaciation fractions (between ~25-80%) within the same temperature range, we observe that the RaFSIPv2 simulation tends to overestimate the median ICNCs predicted by ALLSIP. Indeed, from the normalized histograms of 2D-binned median ICNCs superimposed in Figure 4, we can also infer that RaFSIPv2 predictions can be up to a factor of 3 higher than the ALLSIP predictions, especially in the lower ICNC ranges (e.g., Figure 4d and 4h). In these temperature conditions, only the forestALL and forestBRHM can be activated, with the latter contributing presumably more due to the expected limited presence of large raindrops, which prevents the frequent activation of the forestALL model. The permutation importance of forestBRHM (Figure S7) suggests that RIMC and IWC are the two most important features for the predictions of this model. If higher SIP rates are associated with higher IWC and, hence, glaciation fraction, this could explain the slightly overestimated RaFSIPv2 predictions.

At temperatures below ~ -15 °C, where the relative contribution of PIP starts becoming more important than SIP (Zhao et al., 2023), all three sensitivity experiments produce similar ICNC patterns (Figure 4). The vertical zones of constant median ICNCs observed in all three sensitivity simulations originate from the PIP scheme of WRF being dependent only on temperature (Section 2.1). Nevertheless, reduced ICNCs are simulated during the summer months in ALLSIP (Figure 4n) and RaFSIP (Figure 4o) simulations compared to CONTROL, for clouds formed at temperatures below -18°C and glaciation fractions higher than 40% (upper right part of Figures 4n and 4o). At such low temperatures, the competition between SIP and PIP may limit the amount of water available or the distribution of ice crystals throughout the cloud, thus limiting the ice crystals produced by SIP.

Focusing on the upper right corner of Figure 4, where the temperatures are between -5 and 0°C and the glaciation fraction exceeds 80%, we can observe higher ICNCs simulated by the CONTROL simulation than the two experiments that include SIP parameterizations, especially during Winter and Spring. At temperatures higher than -4°C, elevated ICNCs in the CONTROL experiment can only be explained by ice sedimentation, where precipitating ice particles fall from higher model grid cells. The implementation of SIP in the model can induce numerous ice crystals – albeit with smaller sizes – in the overlying colder clouds or colder parts of the same cloud (Georgakaki et al., 2022; Sotiropoulou et al., 2022). This shift in the ice particle size distribution leads to smaller ice crystals leading to the reduced sedimentation rate of frozen hydrometeors observed in the ALLSIP and RaFSIP simulations. This is further supported by the

joint PDF of the modeled IWC values (Figure S12), where both simulations accounting for SIP result in comparable or even lower IWC values compared to the CONTROL simulation. This can have important implications for the ice and liquid phase partitioning in polar MPCs, determining their microphysical evolution and radiation properties (Curry et al., 1996; Tan & Storelvmo, 2019; Shaw et al., 2022). Overall, the RaFSIP simulation adequately reproduces the most important features in the 2D-binned ICNCs (Figure 4) and IWC (Figure S12) modeled by the ALLSIP simulation, indicating that the newly developed ML parameterization can replicate the underlying physics of the simulation with the detailed SIP microphysics.

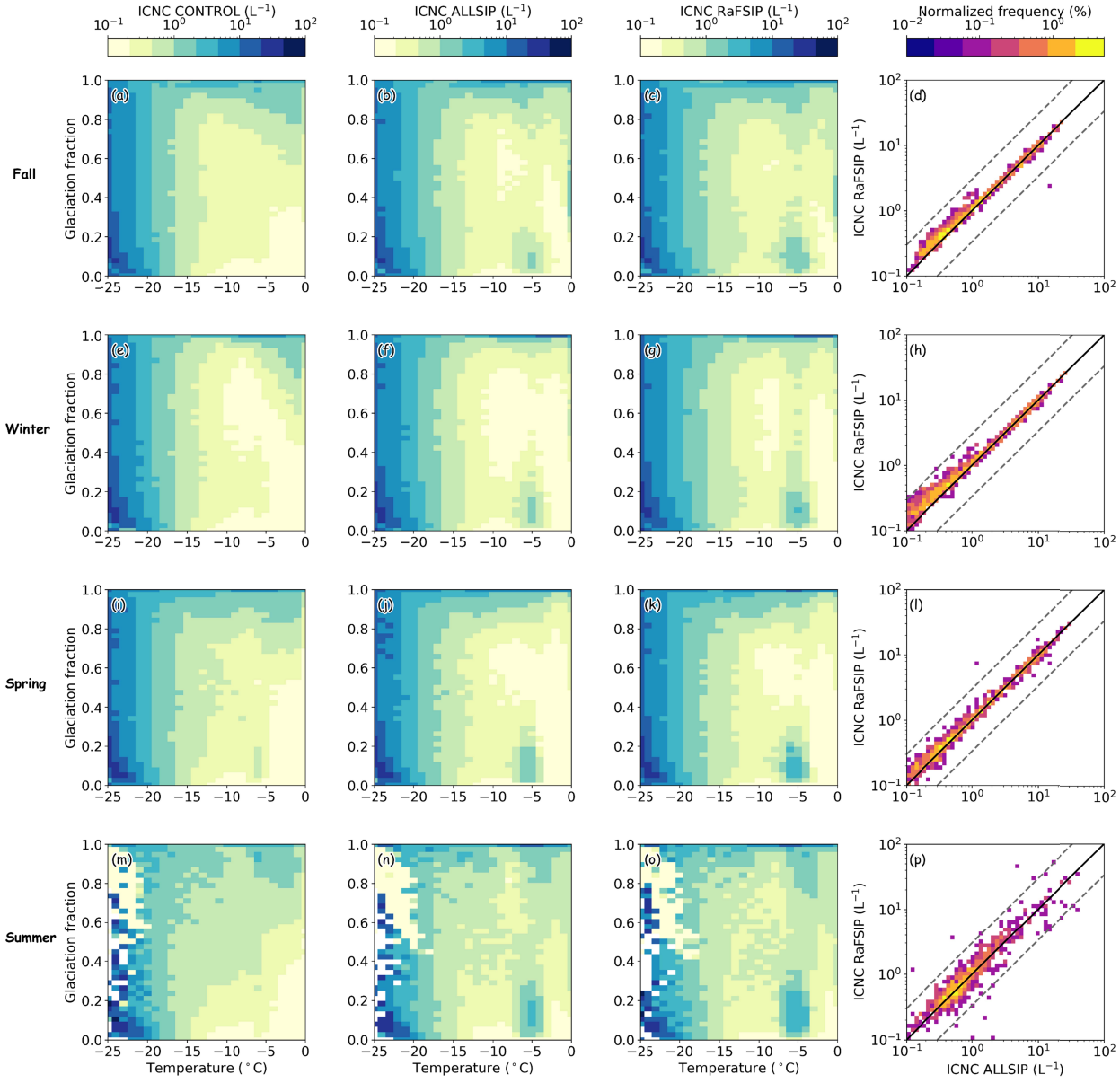

Figure 4. Bivariate joint PDF of median ICNC defined in terms of both temperature and glaciation fraction from the 50-km resolution domain results of the CONTROL (a, e, i, m), ALLSIP (b, f, j, n) and RaFSIPv2 (c, g, k, o) WRF simulations. The normalized histograms of the 2D-binned median ICNC results from the ALLSIP simulation are also plotted versus the

RaFSIPv2 predictions (d, h, l, p). The black line represents the one-to-one line, while the grey dashed lines delimit the area where the ALLSIP values are over or under-estimated by a factor of 3. Statistics are calculated for the 4 simulated seasons: fall (top panel), winter (second panel), spring (third panel) and summer (bottom panel).

Despite the lower R^2 scores in the horizontally averaged ICNCs (Figure S11), replacing the RaFSIPv2 parameterization with RaFSIPv1 in the model leads to comparable results when plotted in the joint temperature-glaciation fraction spectrum (Figure S13). However, the distribution around the 1:1 line is more spread out, especially in spring and summer (Figure S13j and S11p versus Figure 4j and 4p). The main difference between the two approaches is in the very warm subzero temperatures (T>-4°C), where RaFSIPv1 disregards completely the effect of SIP due to the zero PIP rates. As a result, the upper right part of the RaFSIPv1 ICNC distribution is more comparable to the one produced by the CONTROL simulation rather than the ALLSIP simulation (Figure S13).

4.2.2 Median cloud liquid water content

SIP often causes changes in modeled liquid cloud droplets due to increased number concentrations of their frozen counterparts (e.g., Georgakaki et al., 2022; Zhao & Liu, 2021). In addition to direct liquid-to-ice mass transitions caused through the HM and/or DS mechanisms, the elevated concentrations of secondarily formed ice particles can further deplete the surrounding liquid phase hydrometeors in MPCs after their initial growth through vapor diffusion, through the action of the Wegener–Bergeron–Findeisen (WBF) or the riming processes. It is therefore essential to investigate how SIP affects the joint PDF of LWC in the ALLSIP simulation and whether the RaFSIP simulation can reproduce the results.

From the complex patterns of LWC produced (Figure 5), we can infer the non-linearity of the microphysical interactions occurring in mixed-phase and ice clouds. The competition between the two cloud phases is highlighted by the decreasing cloud LWC as the glaciation fraction increases at a given temperature. The dark blue shades confined in the lower part of Figure5, indicate a persistent supercooled liquid layer present in all three sensitivity simulations at temperatures below ~ -4°C with a degree of glaciation below 20% in all seasons except summer, where in the CONTROL simulation it extends up to almost 40% (Figure 5m). This remark can be consistent with the typical structure of high-latitude MPCs, comprising single or multiple stratiform layers of supercooled liquid water from which ice crystals form and precipitate (e.g., Morrison et al., 2012; Shupe, 2011). Including SIP in the simulations slightly restricts the extent of this liquid layer to lower glaciation fractions in both ALLSIP and RaFSIP, most notably during the summer months.

At higher temperatures (>-4°C) and glaciation fraction (>80%), the CONTROL simulation predicts higher LWC values in the region with the elevated ICNCs caused by more frequent ice seeding events (i.e., upper right part of Figure 4a). The presence of more massive precipitating ice particles, indicated by higher IWC values in this region (Figure S12a, e, I, m), sediment quickly and constrains their ability to compete with supercooled liquid water for the available water vapor. In the same region, the ALLSIP and RaFSIP simulations predict lower contribution from both the liquid (Figure 5) and the ice hydrometeors (Figure 4 and S12).

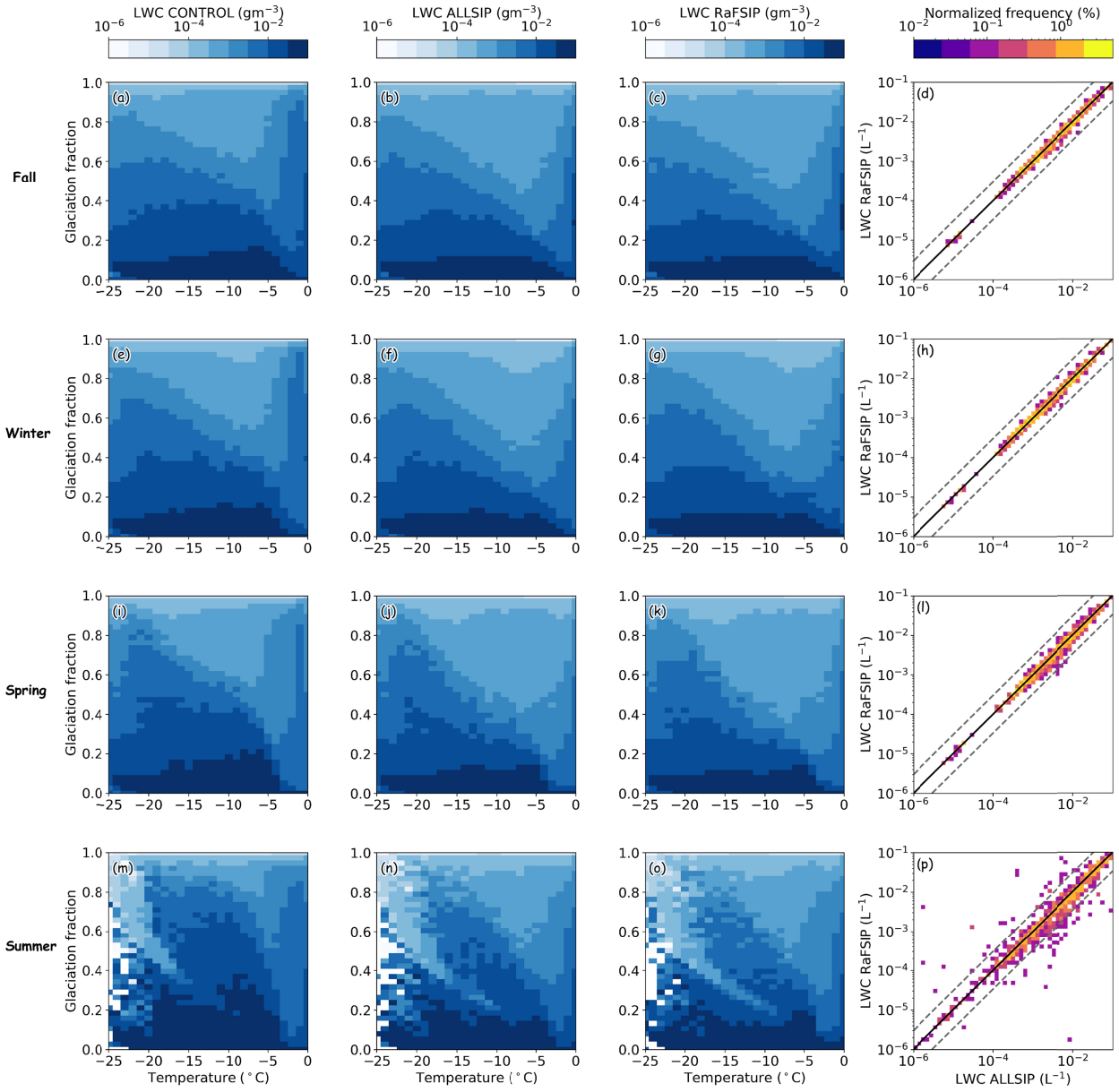

Figure 5. Bivariate joint PDF of median LWC defined in terms of both temperature and glaciation fraction from the 50-km resolution domain results of the CONTROL (a, e, i, m), ALLSIP (b, f, j, n) and RaFSIPv2 (c, g, k, o) WRF simulations. The normalized histograms of the 2D-binned median LWC results from the ALLSIP simulation are also plotted versus the RaFSIPv2 predictions (d, h, l, p). The black line represents the one-to-one line, while the grey dashed lines delimit the area where the ALLSIP values are over or under-estimated by a factor of 3. Statistics are calculated for the 4 simulated seasons: fall (top panel), winter (second panel), spring (third panel) and summer (bottom panel).

By incorporating SIP into the WRF model, polar MPCs are produced with reduced LWC at temperatures above -15°C and glaciation fractions below 60%. In the CONTROL simulation, for instance, during fall and spring, a drop in the simulated LWC to ~10^{-4} gm^{-3} requires

777 temperatures around -8°C and glaciation fraction exceeding 60% (Figure 5a, i). However, in the
778 ALLSIP (Figure 5b, j) and RaFSIP (Figure 5c, k) simulations, such low LWC values can be
779 attained in clouds with a degree of glaciation as low as 40%. The regions of significant ice
780 enhancement in the ALLSIP and RaFSIP simulations (i.e., turquoise bands in Figure 4) do not
781 overlap with the regions of decreased LWC in Figure 5. This can be explained by the time
782 needed for small secondary ice particles to grow first through vapor diffusion until the vapor
783 pressure drops below saturation with respect to liquid water. As the glaciation fraction increases,
784 they can gain mass more efficiently at the expense of the surrounding evaporating cloud droplets
785 (WBF) or through their collection and subsequent freezing (i.e., riming). Both simulations
786 accounting for SIP show remarkable agreement in the location of the most significant ice
787 enhancement (Figure 4), followed by depletion of the mass of supercooled water (Figure 5).

788 At temperatures $\lesssim$-15°C, PIP can contribute significantly to the total ice crystal
789 production rates, leading to a further decrease in LWC through heterogeneous freezing. The
790 combination of heterogeneous freezing, WBF, riming and SIP likely controls the complex LWC
791 patterns observed between -20°C and -4°C. Despite the complexity of the simulated system, the
792 RaFSIP predictions align closely with the 1:1 line in the produced normalized histograms,
793 particularly during fall and winter (Figure 5d and 5h), indicating excellent agreement with the
794 ALLSIP simulation. These findings suggest that the RaFSIP parameterization can accurately
795 capture the cloud phase partitioning produced by the ALLSIP simulation, with an uncertainty of
796 up to a factor of 3. The LWC results from the RaFSIPv1 parameterization (Figure S14)
797 demonstrate that the use of the IEF for parameterizing the effects of SIP also has sufficient
798 predictive skill in WRF. The main difference lies again at warmer temperatures, where the
799 RaFSIPv1 results in slightly overestimated LWC compared to the ALLSIP predictions,
800 especially during fall and winter.
801

802 4.3. Cloud radiative forcing at the surface

803 The preceding discussion illustrates how SIP can significantly alter the number
804 concentration and size distribution of ice and liquid particles in polar MPCs. Such changes in the
805 macro- and microphysical properties of clouds are expected to impact the two most critical cloud
806 feedbacks associated with the polar regions: the cloud optical depth and the cloud-sea-ice
807 feedbacks (e.g., Goosse et al., 2018). For instance, changes in the albedo of MPCs resulting from
808 an increase in the amount of small liquid droplets contained in them can lead to enhanced
809 shortwave radiation reflected back to space and reduced warming at the surface (Murray et al.,
810 2021; Tan & Storelvmo, 2019). During the polar night, however, an increase in low-level cloud
811 coverage has been found to increase the longwave radiation emitted to the surface that is trapped
812 as heat due to the stable stratification conditions in the Arctic, ultimately resulting in surface
813 warming (Ebell et al., 2020; Kay et al., 2016). In this section, we aim to evaluate the
814 performance of the RaFSIP parameterization concerning the anomalies observed in the simulated
815 cloud radiative forcing at the surface (CRF_{surf}) with respect to the ALLSIP simulation (ΔCRF_{surf},
816 Figure 6). The calculations of CRF_{surf} and ΔCRF_{surf} are elaborated in supporting information of
817 Young et al. (2019), which also accounts for additional modifications in the shortwave fluxes to
818 account for the highly reflective Arctic surface (Vavrus, 2006).

819 Figure 6 illustrates the annual cycle of the cloud impact on the surface radiative energy
820 budget, with blue (red) shades indicating cloud-induced cooling (warming). The polar clouds

have a strong longwave greenhouse warming effect during the non-summer months, with the maximum CRF_{surf} reaching up to ~40 Wm^{-2} and locally up to ~60 Wm^{-2} during fall and winter (Figure 6a, b). Ground-based remote sensing observations collected at Ny-Ålesund over two years (2016-2018) found positive monthly net CRF_{surf} between September and April/May, with a mean longwave warming of ~50 Wm^{-2}, which is in line with our results (Ebell et al., 2020). In contrast, during summer, the higher occurrence of liquid in the simulated polar clouds (Figure 5n) combined with the lower surface albedo leads to a strong cloud-induced cooling at the surface by up to ~-100 Wm^{-2} (Figure 6d), again in agreement with Ebell et al. (2020). During spring, the polar clouds have almost a neutral effect over the sea-ice and a slight cooling effect over the open ocean in the lower latitudes (Figure 6c).

The anomalies in longwave and shortwave radiation are calculated by the mean differences in the corresponding predictions between RaFSIP and ALLSIP, the combination of which produced the final surface anomalies, ΔCRF_{surf} (Young et al., 2019). Note that the mean ΔCRF_{surf}, is projected onto a 49 × 49 mesh by averaging over 3 × 3 sub-grids, similar to the averaged maps shown in Figure 3. For the interpretation of ΔCRF_{surf}, the red (blue) colors indicate that more (less) shortwave radiation is reaching the ground in the RaFSIP simulation, which in turn implies the presence of more (less) glaciated clouds than in ALLSIP. Replacing the detailed inline parameterizations of SIP in the M05 scheme with the new RaFSIP parameterization can lead to CRF_{surf} biases between -2.5 and 2.5 Wm^{-2}, with a non-uniform pattern across the model domain (Figures 6e-6h). Compared to the CRF_{surf} magnitudes illustrated in Figure 6, such radiative biases can be considered negligible.

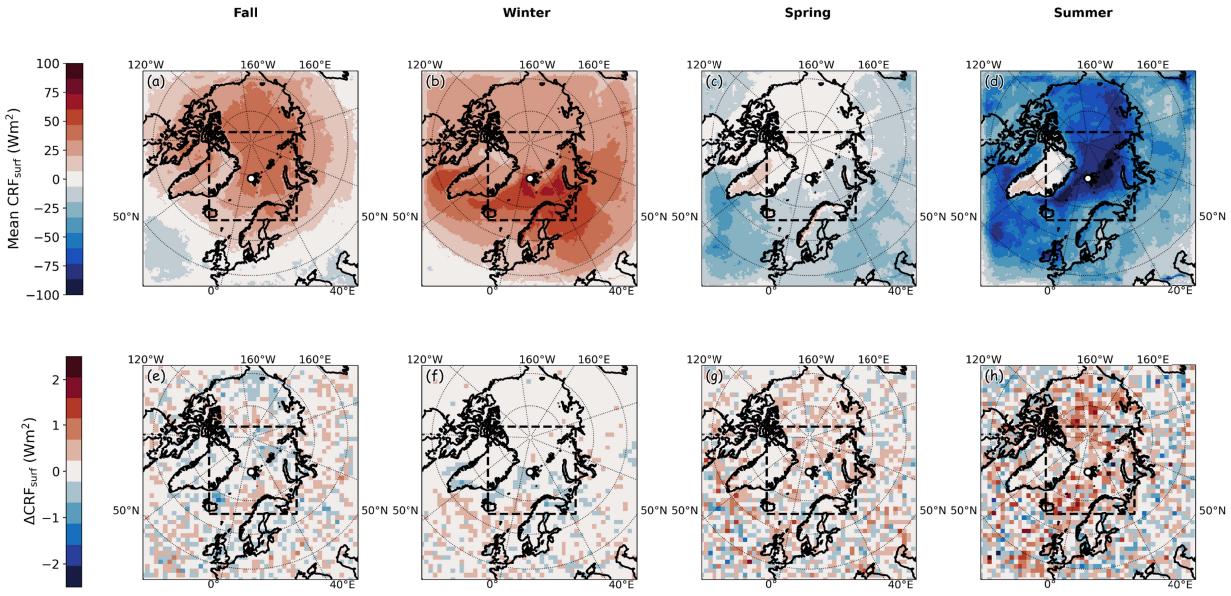

Figure 6. Latitude-longitude maps of (top panel): seasonally-averaged cloud radiative forcing at the surface (CRF_{surf}) simulated by the ALLSIP simulation, and (bottom panel): anomalies with respect to the ALLSIP simulation (ΔCRE_{surf}) derived from the WRF simulation coupled with the RaFSIPv2 parameterization, extracted respectively for (a, e) fall, (b, f) winter, (c, g) spring and (d, h) summer.

During summer, when ice enhancement from SIP is the strongest (Table 3), the largest ΔCRF_{surf} values are largely observed over the sea-ice and ocean grid cells at latitudes higher than 70°N (Figure 6h). At this time, the RaFSIPv2 predictions of the ice (Figure 4p) and liquid (Figure 5p) cloud phase partitioning can be biased by up to a factor of 3, leading to an underestimation of the liquid-dominating clouds compared to ALLSIP, and consequently, an excess of up to ~2.5 Wm^{-2} of shortwave radiation at the surface. However, in the continental and ocean regions of lower latitudes, mostly negative CRF_{surf} biases are observed, indicating that RaFSIPv2 is lacking some ICNCs compared to ALLSIP there. A similar ΔCRF_{surf} pattern characterizes spring (Figure 6g), with the colors shifted towards lighter tones, indicating relatively smaller radiative errors (between -1.5 and 1.5 Wm^{-2}). Fall exhibits a cooling effect (down to -1 Wm^{-2}), with some localized areas of warming (~1 Wm^{-2}) spread around the WRF domain (Figure 6e), while winter is the season with the minimum SIP contribution and the smallest cloud radiative biases, confined mostly to the bottom part of the model domain (Figure 6f).

Figure S15 displays the outcome of the WRF simulations using RaFSIPv1 as a substitute for the RaFSIPv2 parameterization. The obtained ΔCRF_{surf} ranges from -3 to 3 Wm^{-2}, indicating slightly higher radiative biases in all seasons compared to the results shown in Figure 6. The differences between the two SIP parameterizations are most significant in the warm season (Figure S15g and h), where all the positive biases resulting from RaFSIPv2 are replaced by negative ones. The most considerable negative bias appears in the sea area to the east of Greenland (latitudes between 70-80°N), where ~3 Wm^{-2} less shortwave radiation reaches the surface during summer (Figure S15h) compared to the ALLSIP simulation, indicating the tendency of RaFSIPv1 to overestimate the amount of liquid hydrometeors in the summer MPCs. Its reduced predictive ability to capture all the enhanced SIP events present in the ALLSIP simulation stems mainly from the fact that it is limited by the presence of PIP, and hence it cannot be activated for the whole range of conditions that would favor ice multiplication.

5 Summary and outlook

This study introduces a new ML-based framework aimed at representing the impact of ice multiplication in stratiform MPCs within large-scale models. The new RF parameterization, referred to as RaFSIP, is developed using two different approaches to describe the effect of SIP at temperatures as low as -25°C. The first approach indirectly describes SIP through the use of an ice multiplication factor applied to the primary ice production rates, while the second approach directly predicts the SIP tendencies, providing a more explicit representation of the underlying physical processes. RaFSIP is trained on two years of 10-km horizontal resolution WRF simulations over the pan-Arctic region. We evaluate the parameterization both offline and online, and demonstrate that RaFSIP can accurately predict tendencies of unresolved physics in the 50-km horizontal resolution domain, comparable to the conventional SIP schemes. RaFSIP skillfully captures how SIP affects the glaciation state and evolution of polar stratiform MPCs, predicting their ice- and liquid-phase partitioning with an uncertainty of less than a factor of 3. Importantly, RaFSIP exhibits only minor radiative biases, not exceeding ±3 Wm^{-2} at the climatologically-sensitive Arctic surface. This implies that biases in the predicted SIP_{rate} or IEF (depending on the version of RaFSIP used) do not translate into significant errors in simulated cloud microphysical properties and cloud radiative forcing.

The intrinsic property of RF algorithms to make conservative predictions by averaging over the predictions of the individual decision trees allowed the coupled WRF-RaFSIP scheme to run efficiently and without instabilities for a year. The key advantage of our approach is that SIP can be represented using inputs, such as temperature, ice- and liquid water content, riming tendencies, and relative humidity with respect to ice, which are commonly predicted by most models. This facilitates its integration in host models with horizontal grid spacings comparable to or larger than the 10-km resolution grid used for training RaFSIP. This is crucial, as SIP can significantly impact cloud evolution, rapidly glaciating them, altering precipitation and eventually climate.

The incorporation of the RaFSIP framework in the microphysics scheme of 3 GCMs, namely ECHAM-HAM, NorESM2, and EC-Earth, participating in the CMIP assessments is one of the undergoing studies we are currently addressing (Ickes et al., 2023; Costa-Surós et al., 2023). The modular nature of the new SIP parameterization allows for seamless integration with the dynamical core of each GCM model, provided that the input features are well located inside the stratiform cloud microphysics routine. Preliminary results indicate that utilizing grid-box averaged atmospheric variables predicted by GCMs as inputs to the RaFSIP scheme, leads to computationally efficient simulations without numerical instabilities or explosive SIP (not shown). This model intercomparison project will evaluate the robustness of our approach as well as any potential limitations.

As the RaFSIP scheme is trained on a wide range of stratiform conditions where SIP is likely to occur, it can effectively capture the underlying mechanisms behind ice multiplication in any type of single or multi-layered clouds in the polar regions. The limitations for our work stem mostly from the fact that RaFSIP is trained based on regional simulations, and it therefore may not be applicable for the entire globe (e.g., tropical marine or deep convective clouds). To address this, the training dataset can be expanded by incorporating simulation results from various locations worldwide where SIP is recognized (Hoose, 2022). Additionally, the dataset can be augmented to include the description of other SIP processes, such as fragmentation during ice particle sublimation under ice subsaturated cloudy conditions (e.g., Deshmukh et al., 2022). Our study demonstrates that by leveraging a relatively small number of grid points from the regional climate modeling framework, the training dataset can effectively encompass a broader range of cases not covered in our initial analysis.

Finally, this study highlights the significant potential of ML techniques and high-resolution data for the development of computationally efficient and accurate subgrid-scale parameterizations of cloud microphysical processes, addressing the current gaps and limitations in large-scale models. By integrating physics-guided ML algorithms and utilizing feature importance metrics, we increase the transparency of the inner workings of these algorithms, even if they are initially considered uninterpretable (Beucler et al., 2021; McGovern et al., 2019). This is a promising pathway towards model simplification and improved process representation within GCMs. Moving forward, further exploration and implementation of such techniques can contribute to advancements in GCMs, ultimately leading to more robust and comprehensive climate simulations.

Acknowledgments

Funding for this study was provided by the European Research Council (ERC) project "PyroTRACH" (Grant agreement No. 726165) and the European Union's Horizon 2020 project "FORCeS" (Grant agreement No. 821205). The authors thank Dr. Georgia Sotiropoulou for her support providing the version of WRF with explicit SIP cloud microphysics.

Open Research

This manuscript uses the Weather Research and Forecasting model version 4.0.1, which can be accessed at (https://github.com/wrf-model/WRF). The raw WRF outputs reach several terabytes in size, and can be obtained upon request from the corresponding authors. The codes and training dataset for the development of RaFSIP, along with the updated WRF microphysics routines and result analysis, will be made publicly available at https://github.com/pgeorgakaki/RaFSIP upon publication.

References

Abdelwares, M., Haggag, M., Wagdy, A., & Lelieveld, J. (2018). Customized framework of the WRF model for regional climate simulation over the Eastern NILE basin. *Theoretical and Applied Climatology*, *134*(3–4), 1135–1151. https://doi.org/10.1007/s00704-017-2331-2

Atlas, R. L., Bretherton, C. S., Blossey, P. N., Gettelman, A., Bardeen, C., Lin, P., & Ming, Y. (2020). How Well Do Large-Eddy Simulations and Global Climate Models Represent Observed Boundary Layer Structures and Low Clouds Over the Summertime Southern Ocean? *Journal of Advances in Modeling Earth Systems*, *12*(11), 1–25. https://doi.org/10.1029/2020MS002205

Balaji, V., Couvreux, F., Deshayes, J., Gautrais, J., Hourdin, F., & Rio, C. (2022). Are general

960 circulation models obsolete? *Proceedings of the National Academy of Sciences of the*
961 *United States of America*, *119*(47), 1–10. https://doi.org/10.1073/pnas.2202075119
962 Barrett, A. I., Westbrook, C. D., Nicol, J. C., & Stein, T. H. M. (2019). Rapid ice aggregation
963 process revealed through triple-wavelength Doppler spectrum radar analysis. *Atmospheric*
964 *Chemistry and Physics*, *19*(8), 5753–5769. https://doi.org/10.5194/acp-19-5753-2019
965 Beucler, T., Ebert-Uphoff, I., Rasp, S., Pritchard, M., & Gentine, P. (2021). Machine Learning
966 for Clouds and Climate (Invited Chapter for the AGU Geophysical Monograph Series
967 "Clouds and Climate") (Ml). Retrieved from https://doi.org/10.1002/essoar.10506925.1
968 Bigg, E. K. (1953). The supercooling of water. *Proceedings of the Physical Society. Section B*,
969 *66*(8), 688–694. https://doi.org/10.1088/0370-1301/66/8/309
970 de Boer, G., Eloranta, E. W., & Shupe, M. D. (2009). Arctic mixed-phase stratiform cloud
971 properties from multiple years of surface-based measurements at two high-latitude
972 locations. *Journal of the Atmospheric Sciences*, *66*(9), 2874–2887.
973 https://doi.org/10.1175/2009JAS3029.1
974 Breiman, L. (2001). Random forests. *Machine Learning*, *45*, 5–32.
975 https://doi.org/10.1023/A:1010933404324
976 Brenowitz, N. D., & Bretherton, C. S. (2018). Prognostic Validation of a Neural Network
977 Unified Physics Parameterization. *Geophysical Research Letters*, *45*(12), 6289–6298.
978 https://doi.org/10.1029/2018GL078510
979 Brenowitz, N. D., & Bretherton, C. S. (2019). Spatially Extended Tests of a Neural Network
980 Parametrization Trained by Coarse-Graining. *Journal of Advances in Modeling Earth*
981 *Systems*, *11*(8), 2728–2744. https://doi.org/10.1029/2019MS001711
982 Chellini, G., Gierens, R., & Kneifel, S. (2022). Ice Aggregation in Low-Level Mixed-Phase

983 Clouds at a High Arctic Site: Enhanced by Dendritic Growth and Absent Close to the
984 Melting Level. *Journal of Geophysical Research: Atmospheres*, *127*(16), 1–23.
985 https://doi.org/10.1029/2022JD036860
986 Chen, F., & Dudhia, J. (2001). Coupling and advanced land surface-hydrology model with the
987 Penn State-NCAR MM5 modeling system. Part I: Model implementation and sensitivity.
988 *Monthly Weather Review*, *129*(4), 569–585. https://doi.org/10.1175/1520-
989 0493(2001)129<0569:CAALSH>2.0.CO;2
990 Chiu, J. C., Yang, C. K., van Leeuwen, P. J., Feingold, G., Wood, R., Blanchard, Y., et al.
991 (2021). Observational Constraints on Warm Cloud Microphysical Processes Using Machine
992 Learning and Optimization Techniques. *Geophysical Research Letters*, *48*(2), 1–13.
993 https://doi.org/10.1029/2020GL091236
994 Choularton, T. W., Griggs, D. J., Humood, B. Y., & Latham, J. (1980). Laboratory studies of
995 riming, and its relation to ice splinter production. *Quarterly Journal of the Royal*
996 *Meteorological Society*, *106*(448), 367–374. https://doi.org/10.1002/qj.49710644809
997 Cooper, W. A. (1986). Ice Initiation in Natural Clouds. *Meteorological Monographs*, *21*, 29–32.
998 https://doi.org/10.1175/0065-9401-21.43.29
999 Costa-Surós, M., Gonçalves, M., Chatziparaschos, M., Georgakaki, P., Ilić, L., Montane, G.,
1000 Myriokefalitakis, S., van Noije, T., Le Sager, P., Kanakidou, M., Nenes, A., and Pérez
1001 García-Pando, C. (2023). New Aerosol-sensitive Heterogeneous Ice Nucleation
1002 Parameterization in the EC-Earth3 Earth System Model: evaluation and climate response,
1003 EGU General Assembly 2023, Vienna, Austria, 24–28 Apr 2023, EGU23-13040,
1004 https://doi.org/10.5194/egusphere-egu23-13040
1005 Cotton, W. R., Tripoli, G. J., Rauber, R. M., & Mulvihill, E. A. (1986). Numerical Simulation of

1006 the Effects of Varying Ice Crystal Nucleation Rates and Aggregation Processes on
1007 Orographic Snowfall. *Journal of Climate and Applied Meteorology*, *25*(11), 1658–1680.
1008 https://doi.org/10.1175/1520- 780 0450(1986)025<1658:NSOTEO>2.0.CO;2
1009 Curry, J. A., Rossow, W. B., Randall, D., & Schramm, J. L. (1996). Overview of arctic cloud and
1010 radiation characteristics. *Journal of Climate*. https://doi.org/10.1175/1520-
1011 0442(1996)009<1731:OOACAR>2.0.CO;2
1012 Deshmukh, A., Phillips, V. T. J., Bansemer, A., Patade, S., & Waman, D. (2022). New Empirical
1013 Formulation for the Sublimational Breakup of Graupel and Dendritic Snow. *Journal of the*
1014 *Atmospheric Sciences*, *79*(1), 317–336. https://doi.org/10.1175/JAS-D-20-0275.1
1015 Ebell, K., Nomokonova, T., Maturilli, M., & Ritter, C. (2020). Radiative effect of clouds at ny-
1016 Ålesund, svalbard, as inferred from ground-based remote sensing observations. *Journal of*
1017 *Applied Meteorology and Climatology*, *59*(1), 3–22. https://doi.org/10.1175/JAMC-D-19-
1018 0080.1
1019 Field, P. R., Lawson, R. P., Brown, P. R. A., Lloyd, G., Westbrook, C., Moisseev, D., et al.
1020 (2017). Chapter 7. Secondary Ice Production - current state of the science and
1021 recommendations for the future. *Meteorological Monographs*.
1022 https://doi.org/10.1175/amsmonographs-d-16-0014.1
1023 Gentine, P., Pritchard, M., Rasp, S., Reinaudi, G., & Yacalis, G. (2018). Could Machine
1024 Learning Break the Convection Parameterization Deadlock? *Geophysical Research Letters*,
1025 *45*(11), 5742–5751. https://doi.org/10.1029/2018GL078202
1026 Georgakaki, P., Sotiropoulou, G., Vignon, É., Billault-Roux, A. C., Berne, A., & Nenes, A.
1027 (2022). Secondary ice production processes in wintertime alpine mixed-phase clouds.
1028 *Atmospheric Chemistry and Physics*, *22*(3), 1965–1988. https://doi.org/10.5194/acp-22-

1965-2022

Gettelman, A., Gagne, D. J., Chen, C. C., Christensen, M. W., Lebo, Z. J., Morrison, H., & Gantos, G. (2021). Machine Learning the Warm Rain Process. *Journal of Advances in Modeling Earth Systems*, *13*(2). https://doi.org/10.1029/2020MS002268

Goosse, H., Kay, J. E., Armour, K. C., Bodas-Salcedo, A., Chepfer, H., Docquier, D., et al. (2018). Quantifying climate feedbacks in polar regions. *Nature Communications*, *9*(1). https://doi.org/10.1038/s41467-018-04173-0

Grundner, A., Beucler, T., Gentine, P., Iglesias-Suarez, F., Giorgetta, M. A., & Eyring, V. (2022). Deep Learning Based Cloud Cover Parameterization for ICON. *Journal of Advances in Modeling Earth Systems*, *14*(12), 1–24. https://doi.org/10.1029/2021MS002959

Hallett, J., & Mossop, S. C. (1974). Production of secondary ice particles during the riming process. *Nature*, *249*, 26–28. https://doi.org/10.1038/249026a0

Han, Y., Zhang, G. J., Huang, X., & Wang, Y. (2020). A Moist Physics Parameterization Based on Deep Learning. *Journal of Advances in Modeling Earth Systems*, *12*(9). https://doi.org/10.1029/2020MS002076

Hersbach, H., Bell, B., Berrisford, P., Hirahara, S., Horányi, A., Muñoz-Sabater, J., et al. (2020). The ERA5 global reanalysis. *Quarterly Journal of the Royal Meteorological Society*, *146*(730), 1999–2049. https://doi.org/10.1002/qj.3803

Hoose, C. (2022). Another Piece of Evidence for Important but Uncertain Ice Multiplication Processes. *AGU Advances*, *3*(2), 2021–2023. https://doi.org/10.1029/2022AV000669

Hourdin, F., Mauritsen, T., Gettelman, A., Golaz, J. C., Balaji, V., Duan, Q., et al. (2017). The art and science of climate model tuning. *Bulletin of the American Meteorological Society*, *98*(3), 589–602. https://doi.org/10.1175/BAMS-D-15-00135.1

1052 Ickes, L., Costa Surós, M., Eriksson, P., Frostenberg, H., Georgakaki, P., Gonçalves Ageitos, M.,
1053 Hallborn, H., Lewinschal, A., May, E., Nenes, A., Neubauer, D., Pérez García-Pando, C.,
1054 Proske, U., and Sotiropoulou, G. (2023). How important are secondary ice processes –
1055 preliminary results from FOR-ICE, EGU General Assembly 2023, Vienna, Austria, 24–28
1056 Apr 2023, EGU23-10696, https://doi.org/10.5194/egusphere-egu23-10696.
1057 Irrgang, C., Boers, N., Sonnewald, M., Barnes, E. A., Kadow, C., Staneva, J., & Saynisch-
1058 Wagner, J. (2021). Towards neural Earth system modelling by integrating artificial
1059 intelligence in Earth system science. *Nature Machine Intelligence*, *3*(8), 667–674.
1060 https://doi.org/10.1038/s42256-021-00374-3
1061 James, R. L., Phillips, V. T. J., & Connolly, P. J. (2021). Secondary ice production during the
1062 break-up of freezing water drops on impact with ice particles. *Atmospheric Chemistry and*
1063 *Physics*, *21*(24), 18519–18530. https://doi.org/10.5194/acp-21-18519-2021
1064 Järvinen, E., McCluskey, C. S., Waitz, F., Schnaiter, M., Bansemer, A., Bardeen, C. G., et al.
1065 (2022). Evidence for Secondary Ice Production in Southern Ocean Maritime Boundary
1066 Layer Clouds. *Journal of Geophysical Research: Atmospheres*, *127*(16), 1–31.
1067 https://doi.org/10.1029/2021JD036411
1068 Karalis, M., Sotiropoulou, G., Abel, S. J., Bossioli, E., Georgakaki, P., Methymaki, G., et al.
1069 (2022). Effects of secondary ice processes on a stratocumulus to cumulus transition during a
1070 cold-air outbreak. *Atmospheric Research*, *277*.
1071 https://doi.org/10.1016/j.atmosres.2022.106302
1072 Kay, J. E., L'Ecuyer, T., Chepfer, H., Loeb, N., Morrison, A., & Cesana, G. (2016). Recent
1073 Advances in Arctic Cloud and Climate Research. *Current Climate Change Reports*, *2*(4),
1074 159–169. https://doi.org/10.1007/s40641-016-0051-9

1075 Kleinheins, J., Kiselev, A., Keinert, A., Kind, M., & Leisner, T. (2021). Thermal imaging of
1076 freezing drizzle droplets: pressure release events as a source of secondary ice particles.
1077 *Journal of the Atmospheric Sciences*, 1–28. https://doi.org/10.1175/jas-d-20-0323.1
1078 Korolev, A., & Leisner, T. (2020). *Review of experimental studies of secondary ice production*.
1079 *Atmospheric Chemistry and Physics* (Vol. 20). https://doi.org/10.5194/acp-20-11767-2020
1080 Korolev, A., Heckman, I., Wolde, M., Ackerman, A. S., Fridlind, A. M., Ladino, L. A., et al.
1081 (2020). A new look at the environmental conditions favorable to secondary ice production.
1082 *Atmospheric Chemistry and Physics*, *20*(3), 1391–1429. https://doi.org/10.5194/acp-20-
1083 1391-2020
1084 Korolev, A., Demott, P. J., Heckman, I., Wolde, M., Williams, E., Smalley, D. J., & Donovan,
1085 M. F. (2022). Observation of secondary ice production in clouds at low temperatures.
1086 *Atmospheric Chemistry and Physics*, *22*(19), 13103–13113. https://doi.org/10.5194/acp-22-
1087 13103-2022
1088 Lauber, A., Henneberger, J., Mignani, C., Ramelli, F., Pasquier, J. T., Wieder, J., et al. (2021).
1089 Continuous secondary-ice production initiated by updrafts through the melting layer in
1090 mountainous regions. *Atmospheric Chemistry and Physics*, *21*(5), 3855–3870.
1091 https://doi.org/10.5194/acp-21-3855-2021
1092 Liu, Y., Yau, M. K., Shima, S. ichiro, Lu, C., & Chen, S. (2023). Parameterization and Explicit
1093 Modeling of Cloud Microphysics: Approaches, Challenges, and Future Directions.
1094 *Advances in Atmospheric Sciences*, *40*(5), 747–790. https://doi.org/10.1007/s00376-022-
1095 2077-3
1096 Luke, E. P., Yang, F., Kollias, P., Vogelmann, A. M., & Maahn, M. (2021). New insights into ice
1097 multiplication using remote-sensing observations of slightly supercooled mixed-phase

clouds in the Arctic. *Proceedings of the National Academy of Sciences of the United States of America*, *118*(13), 1–9. https://doi.org/10.1073/pnas.2021387118

McCoy, I. L., McCoy, D. T., Wood, R., Regayre, L., Watson-Parris, D., Grosvenor, D. P., et al. (2020). The hemispheric contrast in cloud microphysical properties constrains aerosol forcing. *Proceedings of the National Academy of Sciences of the United States of America*, *117*(32), 18998–19006. https://doi.org/10.1073/pnas.1922502117

McGovern, A., Lagerquist, R., Gagne, D. J., Jergensen, G. E., Elmore, K. L., Homeyer, C. R., & Smith, T. (2019). Making the black box more transparent: Understanding the physical implications of machine learning. *Bulletin of the American Meteorological Society*, *100*(11), 2175–2199. https://doi.org/10.1175/BAMS-D-18-0195.1

Meyers, M. P., DeMott, P. J., & Cotton, W. R. (1992). New Primary Ice-Nucleation Parameterizations in an Explicit Cloud Model. *Journal of Applied Meteorology*, *31*, 708–721. https://doi.org/10.1175/1520- 0450(1992)031<0708:NPINPI>2.0.CO;2

Mooers, G., Pritchard, M., Beucler, T., Ott, J., Yacalis, G., Baldi, P., & Gentine, P. (2021). Assessing the Potential of Deep Learning for Emulating Cloud Superparameterization in Climate Models With Real-Geography Boundary Conditions. *Journal of Advances in Modeling Earth Systems*, *13*(5), 1–26. https://doi.org/10.1029/2020MS002385

Morrison, H., Curry, J. A., & Khvorostyanov, V. I. (2005). A new double-moment microphysics parameterization for application in cloud and climate models. Part I: Description. *Journal of the Atmospheric Sciences*, *62*, 1678–1693. https://doi.org/10.1175/JAS3446.1

Morrison, Hugh, De Boer, G., Feingold, G., Harrington, J., Shupe, M. D., & Sulia, K. (2012). Resilience of persistent Arctic mixed-phase clouds. *Nature Geoscience*, *5*, 11–17. https://doi.org/10.1038/ngeo1332

1121 Morrison, Hugh, van Lier-Walqui, M., Fridlind, A. M., Grabowski, W. W., Harrington, J. Y.,
1122 Hoose, C., et al. (2020). Confronting the Challenge of Modeling Cloud and Precipitation
1123 Microphysics. *Journal of Advances in Modeling Earth Systems*, *12*(8).
1124 https://doi.org/10.1029/2019MS001689
1125 Murray, B. J., Carslaw, K. S., & Field, P. R. (2021). Opinion: Cloud-phase climate feedback and
1126 the importance of ice-nucleating particles. *Atmospheric Chemistry and Physics*, *21*(2), 665–
1127 679. https://doi.org/10.5194/acp-21-665-2021
1128 Nakanishi, M., & Niino, H. (2006). An improved Mellor-Yamada Level-3 model: Its numerical
1129 stability and application to a regional prediction of advection fog. *Boundary-Layer*
1130 *Meteorology*, *119*(2), 397–407. https://doi.org/10.1007/s10546-005-9030-8
1131 O'Gorman, P. A., & Dwyer, J. G. (2018). Using Machine Learning to Parameterize Moist
1132 Convection: Potential for Modeling of Climate, Climate Change, and Extreme Events.
1133 *Journal of Advances in Modeling Earth Systems*, *10*(10), 2548–2563.
1134 https://doi.org/10.1029/2018ms001351
1135 Papakonstantinou-Presvelou, I., Sourdeval, O., & Quaas, J. (2022). Strong Ocean/Sea-Ice
1136 Contrasts Observed in Satellite-Derived Ice Crystal Number Concentrations in Arctic Ice
1137 Boundary-Layer Clouds. *Geophysical Research Letters*, *49*(13).
1138 https://doi.org/10.1029/2022GL098207
1139 Pasquier, J. T., Henneberger, J., Ramelli, F., Lauber, A., David, R. O., Wieder, J., et al. (2022).
1140 Conditions favorable for secondary ice production in Arctic mixed-phase clouds.
1141 *Atmospheric Chemistry and Physics*, *22*(23), 15579–15601. https://doi.org/10.5194/acp-22-
1142 15579-2022
1143 Pedregosa, F., Varoquaux, G., Gramfort, A., Michel, V., Thirion, B., Grisel, O., et al. (2011).

Scikit-learn: Machine learning in Python. *Journal of Machine Learning Research*, *12*, 2825–2830. https://doi.org/10.1289/EHP4713

Phillips, V. T. J., Yano, J. I., Formenton, M., Ilotoviz, E., Kanawade, V., Kudzotsa, I., et al. (2017). Ice multiplication by breakup in ice-ice collisions. Part II: Numerical simulations. *Journal of the Atmospheric Sciences*, *74*(9), 2789–2811. https://doi.org/10.1175/JAS-D-16-0223.1

Phillips, V. T. J., Patade, S., Gutierrez, J., & Bansemer, A. (2018). Secondary ice production by fragmentation of freezing drops: Formulation and theory. *Journal of the Atmospheric Sciences*, *75*, 3031–3070. https://doi.org/10.1175/JAS-D-17-0190.1

Ramelli, F., Henneberger, J., David, R. O., Bühl, J., Radenz, M., Seifert, P., et al. (2021). Microphysical investigation of the seeder and feeder region of an Alpine mixed-phase cloud. *Atmospheric Chemistry and Physics*, *21*, 6681–6706. https://doi.org/10.5194/acp-21-6681-2021

Rangno, A. L., & Hobbs, P. V. (2001). Ice particles in stratiform clouds in the Arctic and possible mechanisms for the production of high ice concentrations. *Journal of Geophysical Research Atmospheres*, *106*(D14), 15065–15075. https://doi.org/10.1029/2000JD900286

Rasp, S. (2020). Coupled online learning as a way to tackle instabilities and biases in neural network parameterizations : general algorithms and Lorenz 96 case study (v1.0). *Geoscientific Model Development*, *13*, 2185–2196.

Schneider, T., Lan, S., Stuart, A., & Teixeira, J. (2017). Earth System Modeling 2 . 0 : A Blueprint for Models That Learn From Observations and Targeted High-Resolution Simulations. *Geophysical Research Letters*, *44*, 12396–12417. https://doi.org/10.1002/2017GL076101

1167 Schuddeboom, A. J., & McDonald, A. J. (2021). The Southern Ocean Radiative Bias, Cloud
1168 Compensating Errors, and Equilibrium Climate Sensitivity in CMIP6 Models. *Journal of*
1169 *Geophysical Research: Atmospheres*, *126*(22), 1–16. https://doi.org/10.1029/2021JD035310
1170 Schwarzenboeck, A., Shcherbakov, V., Lefevre, R., Gayet, J. F., Pointin, Y., & Duroure, C.
1171 (2009). Indications for stellar-crystal fragmentation in Arctic clouds. *Atmospheric Research*,
1172 *92*(2), 220–228. https://doi.org/10.1016/j.atmosres.2008.10.002
1173 Seifert, A., & Rasp, S. (2020). Potential and Limitations of Machine Learning for Modeling
1174 Warm-Rain Cloud Microphysical Processes. *Journal of Advances in Modeling Earth*
1175 *Systems*, *12*(12). https://doi.org/10.1029/2020MS002301
1176 Shaw, J., McGraw, Z., Bruno, O., Storelvmo, T., & Hofer, S. (2022). Using Satellite
1177 Observations to Evaluate Model Microphysical Representation of Arctic Mixed-Phase
1178 Clouds. *Geophysical Research Letters*, *49*(3), 1–10. https://doi.org/10.1029/2021GL096191
1179 Shupe, M. D. (2011). Clouds at arctic atmospheric observatories. Part II: Thermodynamic phase
1180 characteristics. *Journal of Applied Meteorology and Climatology*, *50*(3), 645–661.
1181 https://doi.org/10.1175/2010JAMC2468.1
1182 Shupe, M. D., Matrosov, S. Y., & Uttal, T. (2006). Arctic Mixed-Phase Cloud Properties
1183 Derived from Surface-Based Sensors at SHEBA. *Journal of the Atmospheric Sciences*,
1184 *63*(2), 697–711. https://doi.org/10.1175/jas3659.1
1185 Sledd, A., & L'Ecuyer, T. (2021). Uncertainty in forced and natural arctic solar absorption
1186 variations in CMIP6 models. *Journal of Climate*, *34*(3), 931–948.
1187 https://doi.org/10.1175/JCLI-D-20-0244.1
1188 Sotiropoulou, G., Sullivan, S., Savre, J., Lloyd, G., Lachlan-Cope, T., Ekman, A. M. L., &
1189 Nenes, A. (2020). The impact of secondary ice production on Arctic stratocumulus.

Atmospheric Chemistry and Physics, *20*, 1301–1316. https://doi.org/10.5194/acp-20-1301-2020

Sotiropoulou, G., Ickes, L., Nenes, A., & Ekman, A. (2021). Ice multiplication from ice–ice collisions in the high Arctic: sensitivity to ice habit, rimed fraction, ice type and uncertainties in the numerical description of the process. *Atmospheric Chemistry and Physics*, *21*, 9741–9760. https://doi.org/10.5194/acp-21-9741-2021

Sotiropoulou, G., Vignon, E., Young, G., Morrison, H., O'Shea, S. J., Lachlan-Cope, T., et al. (2021). Secondary ice production in summer clouds over the Antarctic coast: An underappreciated process in atmospheric models. *Atmospheric Chemistry and Physics*, *21*(2), 755–771. https://doi.org/10.5194/acp-21-755-2021

Sotiropoulou, G., Lewinschal, A., Georgakaki, P., Phillips, V., Patade, S., Ekman, A. M. L., & Nenes, A. (2022). Sensitivity of Arctic clouds to ice microphysical processes in the NorESM2 climate model. *Preprint on Authorea*. https://doi.org/10.1002/essoar.10512081.1

Takahashi, T., Nagao, Y., & Kushiyama, Y. (1995). Possible High Ice Particle Production during Graupel–Graupel Collisions. *Journal of the Atmospheric Sciences*, *52*, 4523–4527.

Tan, I., & Storelvmo, T. (2019). Evidence of Strong Contributions From Mixed-Phase Clouds to Arctic Climate Change. *Geophysical Research Letters*, *46*(5), 2894–2902. https://doi.org/10.1029/2018GL081871

Vardiman, L. (1978). The Generation of Secondary Ice Particles in Clouds by Crystal–Crystal Collision. *Journal of the Atmospheric Sciences*, *35*, 2168–2180. https://doi.org/10.1175/1520- 0469(1978)035<2168:TGOSIP>2.0.CO;2,

Vavrus, S. (2006). An alternative method to calculate cloud radiative forcing: Implications for quantifying cloud feedbacks. *Geophysical Research Letters*, *33*(1), 2–5.

https://doi.org/10.1029/2005GL024723

Vergara-Temprado, J., Miltenberger, A. K., Furtado, K., Grosvenor, D. P., Shipway, B. J., Hill, A. A., et al. (2018). Strong control of Southern Ocean cloud reflectivity by ice-nucleating particles. *Proceedings of the National Academy of Sciences of the United States of America*, *115*(11), 2687–2692. https://doi.org/10.1073/pnas.1721627115

Waman, D., Patade, S., Jadav, A., Deshmukh, A., Gupta, A. K., Phillips, V. T. J., et al. (2022). Dependencies of Four Mechanisms of Secondary Ice Production on Cloud-Top Temperature in a Continental Convective Storm. *Journal of the Atmospheric Sciences*, *79*(12), 3375–3404. https://doi.org/10.1175/JAS-D-21-0278.1

Wex, H., Huang, L., Zhang, W., Hung, H., Traversi, R., Becagli, S., et al. (2019). Annual variability of ice-nucleating particle concentrations at different Arctic locations. *Atmospheric Chemistry and Physics*, *19*(7), 5293–5311. https://doi.org/10.5194/acp-19-5293-2019

Wieder, J., Ihn, N., Mignani, C., Haarig, M., Bühl, J., Seifert, P., et al. (2022). Retrieving ice-nucleating particle concentration and ice multiplication factors using active remote sensing validated by in situ observations. *Atmospheric Chemistry and Physics*, *22*(15), 9767–9797. https://doi.org/10.5194/acp-22-9767-2022

Young, G., Jones, H. M., Choularton, T. W., Crosier, J., Bower, K. N., Gallagher, M. W., et al. (2016). Observed microphysical changes in Arctic mixed-phase clouds when transitioning from sea ice to open ocean. *Atmospheric Chemistry and Physics*, *16*, 13945–13967. https://doi.org/10.5194/acp-16-13945-2016

Young, G., Lachlan-Cope, T., O'Shea, S. J., Dearden, C., Listowski, C., Bower, K. N., et al. (2019). Radiative Effects of Secondary Ice Enhancement in Coastal Antarctic Clouds.

Geophysical Research Letters, *46*, 2312–2321. https://doi.org/10.1029/2018GL080551

Yuval, J., & O'Gorman, P. A. (2020). Stable machine-learning parameterization of subgrid processes for climate modeling at a range of resolutions. *Nature Communications*, *11*(1), 1–10. https://doi.org/10.1038/s41467-020-17142-3

Yuval, J., O'Gorman, P. A., & Hill, C. N. (2021). Use of Neural Networks for Stable , Accurate and Physically Consistent Parameterization of Subgrid Atmospheric Processes With Good Performance at Reduced Precision Geophysical Research Letters. *Geophysical Research Letters*, *48*, 1–11. https://doi.org/10.1029/2020GL091363

Zelinka, M. D., Myers, T. A., McCoy, D. T., Po-Chedley, S., Caldwell, P. M., Ceppi, P., et al. (2020). Causes of Higher Climate Sensitivity in CMIP6 Models. *Geophysical Research Letters*, *47*(1), 1–12. https://doi.org/10.1029/2019GL085782

Zhang, G., & Lu, Y. (2012). Bias-corrected random forests in regression. *Journal of Applied Statistics*, *39*(1), 151–160. https://doi.org/10.1080/02664763.2011.578621

Zhao, X., & Liu, X. (2021). Global Importance of Secondary Ice Production. *Geophysical Research Letters*, *48*(11), 1–11. https://doi.org/10.1029/2021GL092581

Zhao, X. & Liu, X. (2022). Primary and secondary ice production: interactions and their relative importance, *Atmospheric Chemistry and Physics*, *22,* 2585–2600. https://doi.org/10.5194/acp-22-2585-2022

Zhao, X., Liu, X., Burrows, S., DeMott, P. J., Diao, M., McFarquhar, G. M., et al. (2023). Important Ice Processes Are Missed by the Community Earth System Model in Southern Ocean Mixed-Phase Clouds: Bridging SOCRATES Observations to Model Developments. *Journal of Geophysical Research: Atmospheres*, *128*(4), 1–15. https://doi.org/10.1029/2022JD037513

1259